ASTRONOMY & ASTROPHYSICS
SUPPLEMENT SERIES

Astron. Astrophys. Suppl. Ser. **139**, 393–415 (1999)

Young massive star clusters in nearby galaxies⋆,⋆⋆

II. Software tools, data reductions and cluster sizes

S.S. Larsen

Copenhagen University Astronomical Observatory, Juliane Maries Vej 32, 2100 Copenhagen Ø, Denmark
e-mail: soeren@astro.ku.dk

Received March 9; accepted July 5, 1999

Abstract. A detailed description is given of the data analysis leading to the discovery of young massive star clusters (YMCs) in a sample of 21 nearby galaxies. A new useful tool, **ishape**, for the derivation of intrinsic shape parameters of compact objects is presented, and some test results are shown. Completeness tests for the cluster samples are discussed, and **ishape** is used to estimate cluster sizes. Half-light radii of $0-20$ pc are derived for clusters in 2 of the most cluster-rich galaxies, NGC 1313 and NGC 5236, which is within the range spanned by globular clusters in the Milky Way and by YMCs in the LMC and some starburst galaxies. Photometric data for all clusters, along with positions and estimated half-light radii, are tabulated.

Key words: photometry — spiral — star clusters — techniques: image processing

1. Introduction

This paper is the second in a series describing the observations of "young massive star clusters" (YMCs) in a number of nearby spiral and irregular galaxies. A general outline of the project was given by Larsen & Richtler (1999, Paper I), and some first results were presented there. In this paper the data reductions are discussed in more detail, with special emphasis on two software tools developed as part of the project, which may be of general use to the astronomical community. These tools are **mksynth**, a programme which generates synthetic images with realistic noise characteristics, and **ishape** which derives intrinsic shape parameters for compact objects in a digital image by convolving an analytic model profile with the PSF and matching the result to the observed profile.

By YMCs we mean objects of the same type as e.g. the cluster NGC 1866 in the Large Magellanic Cloud (Fischer et al. 1992). They are characterised by being similar (with respect to mass and morphology) to globular clusters seen in the Milky Way, but of much lower ages – in fact, the lower age limit of the clusters in our sample is set only by the fact that we avoid objects located within HII regions.

The paper is organised as follows: The observations are described in Sect. 2, and Sect. 3 is a discussion of the basic data reduction procedure including the standard calibrations. In Sect. 4 the tools **mksynth** and **ishape** are introduced, and Sect. 5 gives a discussion of the completeness corrections used in Paper I. Finally, in Sect. 6 **ishape** is used to derive radii of the clusters, and some implications of the results are discussed.

2. Observations

Observations of 21 nearby galaxies, listed in Table 1 of Paper I, were carried out with the Danish 1.54 m. telescope and DFOSC (Danish Faint Object Spectrograph and Camera) at the European Southern Observatory (ESO) at La Silla, Chile, and with the 2.56 m. Nordic Optical Telescope and ALFOSC (a DFOSC twin instrument), situated at La Palma, Canary Islands. The data consist of CCD images in the filters U, B, V, R, I and Hα. In the filters $BVRI$ and Hα we typically made 3 exposures per galaxy of 5 minutes each, and 3 exposures of 20 minutes each in the U band. V-band images of the galaxies are shown in Figs. 4 and 5.

⋆ Based on observations made with the Nordic Optical Telescope, operated on the island of La Palma jointly by Denmark, Finland, Iceland, Norway, and Sweden, in the Spanish Observatorio del Roque de los Muchachos of the Instituto de Astrofisica de Canarias, and with the Danish 1.5-m telescope at ESO, La Silla, Chile.

⋆⋆ Table 4 is also available in electronic form at the CDS via anonymous ftp (130.79.128.5) or via http://cdsweb.u-strasbg.fr/Abstract.html

Both the ALFOSC and DFOSC were equipped with thinned, backside-illuminated 2 K^2 Loral-Lesser CCDs. The pixel scale in the ALFOSC is 0.189″/pixel and the scale in the DFOSC is 0.40″/pixel, giving field sizes of $6.5' \times 6.5'$ and $13.7' \times 13.7'$, respectively.

The seeing during the observations at La Silla was typically around 1.5 arcseconds as measured on V-band frames. On the images taken with the NOT the seeing was usually about 0.8 arcseconds. All observations used in this paper were conducted under photometric conditions.

During each observing run, photometric standard stars in the Landolt (1992) fields were observed for calibration of the photometry. Care was taken to include standard stars over as wide a range in colours as possible, usually from $B-V \approx -0.15$ to $B-V \approx 1.1$. Some of the Landolt fields were observed several times during the night at different airmass in order to measure the atmospheric extinction coefficients. For the flatfielding we used skyflats exposed to about half the dynamic range of the CCD, and in general each flatfield used in the reductions was constructed as an average of about 5 individual integrations, slightly offset with respect to each other in order to eliminate any stars.

3. Data reduction

The initial reductions of all CCD images (bias subtraction, flatfield correction, removal of bad columns) were done using the standard tools in IRAF[1].

3.1. Standard calibrations

The instrumental magnitudes for the standard stars were obtained on the CCD images using the **phot** task in DAOPHOT (Stetson 1987) with an aperture radius of 20 pixels. The extinction correction was then applied directly to the raw instrumental magnitudes. The standard calibrations were carried out using the **photcal** package in IRAF with the transformation equations assumed to be of the linear form

$$\begin{aligned} V &= v + c_v \times (b-v) + z_v \\ B-V &= c_{(b-v)} \times (b-v) + z_{(b-v)} \\ U-B &= c_{(u-b)} \times (u-b) + z_{(u-b)} \\ V-R &= c_{(v-r)} \times (v-r) + z_{(v-r)} \\ V-I &= c_{(v-i)} \times (v-i) + z_{(v-i)}. \end{aligned}$$

Here the magnitudes written in capital letters correspond to the standard system, and magnitudes written with small letters are in the instrumental system, corrected for extinction only.

[1] IRAF is distributed by the National Optical Astronomical Observatories, which are operated by the Association of Universities for Research in Astronomy, Inc. under contract with the National Science Foundation.

Table 1. The standard transformation coefficients for each of the four observing runs. N is the total number of observations of individual stars used for the transformations. The number of stars N_s actually involved is always smaller, some of the fields being observed several times. The rms values refer to the scatter around the standard transformations

	NOT1	NOT2	DK1	DK2
N_s	14	32	45	35
N	25	69	98	94
c_v	−0.056	−0.034	0.039	0.029
$c_{(b-v)}$	1.109	1.111	1.100	1.104
$c_{(u-b)}$	1.081	1.055	0.943	0.959
$c_{(v-r)}$	1.012	1.027	1.013	1.014
$c_{(v-i)}$	0.919	0.948	1.031	1.045
z_v	−0.699	−0.481	−2.064	−2.094
$z_{(b-v)}$	0.082	0.005	−0.540	−0.432
$z_{(u-b)}$	−1.988	−1.830	−2.118	−2.260
$z_{(v-r)}$	−0.091	−0.086	−0.019	0.154
$z_{(v-i)}$	0.219	0.234	1.065	1.198
rms(V)	0.008	0.034	0.019	0.037
rms($B-V$)	0.013	0.042	0.019	0.032
rms($U-B$)	0.042	0.043	0.050	0.041
rms($V-I$)	0.017	0.033	0.030	0.024

The coefficients of the standard transformation equations are given in Table 1 for each of the four observing runs. NOT1 and NOT2 refer to observing runs at the Nordic Optical Telescope in May 1997 and October 1997, respectively, and DK1 and DK2 refer to runs at the Danish 1.54 m telescope in September 1997 and February 1998. The CCD at the NOT was interchanged between the two runs which may explain the changes in the instrumental system from one run to the other, while the quantum efficiency of the CCD at the 1.54 m telescope was notoriously unstable during the summer 1997/1998, and therefore the changes in the zero-point constants are hardly surprising. The rms scatter of the standard star observations relative to the standard system after the transformation is generally of the order of a few times 0.01 mag, with a slightly larger scatter in the $U-B$ transformation. Thus, the accuracy of the standard transformations is sufficient for our purpose.

3.2. Reduction of science data

Following the initial reductions, the three exposures in each filter were aligned and combined into a single image, yielding an effective integration time of 15 minutes in $BVRI$ and Hα and 60 minutes in U. As both the DFOSC and ALFOSC instruments can be rotated around the optical axis it was sometimes necessary to counter-rotate the individual exposures before they were combined (using the IRAF task **rotate**), even if attempts were made to position the instruments in the same way from night to night. This is due to the limited angular resolution of the encoders on the rotators. The necessary offsets and rotations were

calculated by manually inspecting each frame and measuring the $x - y$ coordinates of two selected stars using the IRAF task **imexamine**. By this method it was possible to align the images to a precision of about 0.1 pixel, accurate enough for our purpose. Flux conservation during the rotation was checked by comparing photometry on a synthetically generated image and on a rotated version of the same image. No deviations larger than 0.003 mag were found.

The actual combination of the individual images was done using the task **imcombine**, with the **reject** option set to **crreject** in order to remove cosmic ray events. It was necessary to be particularly careful if the images to be combined had slightly different seeing, because the centres of bright stars could then be "rejected" by **imcombine**. We checked that this did not happen by also combining the images using no rejection at all and subtracting the two versions of the combined images from each other, making sure that no residuals were seen at the positions of stars. In general it was possible to avoid this problem by adjusting the **snoise** ("sensitivity noise") parameter of **imcombine**.

As the first step towards detecting point-like objects we then created a smoothed version of a V-band image, using the median filtering task in IRAF and a 5×5 pixels box median filter. The median-filtered image was then subtracted from the original version, resulting in a residual image that contained no large-scale structure but only point sources superimposed on a uniform background. Point sources were finally located in the residual image using the **daofind** task in DAOPHOT.

Because star clusters are sometimes seen as slightly extended sources even at the distance of the galaxies in our sample, the photometry had to be obtained as aperture photometry rather than by PSF fitting (see also Östlin et al. 1998). The photometry was carried out directly on the combined images, and not on background subtracted images. In Paper I it was argued that the accuracy obtained by this method was quite satisfactory. An aperture radius of 4 pixels was chosen for the determination of colour indices, while an aperture radius of 8 pixels was used to measure V band magnitudes. It was shown in Paper I (see also e.g. Holtzman et al. 1996) that aperture corrections tend to cancel out for colour indices, thus making it possible to measure accurate colours even with a quite small aperture.

The pixel size on the NOT images is half of that on the 1.54 m. images, but by coincidence the seeing on the NOT data was also, in general, twice as good as on the 1.54 m. data, so we used the same aperture radii in pixels for the NOT and 1.54 m. observations. Aperture corrections relative to the 20-pixels aperture radius used for the standard star observations were applied to the photometry, based on the assumption that the objects were point sources. The aperture corrections were derived from photometry of a few bright, isolated stars using the **mkapfile** task in DAOPHOT, and amounted in general to a few tenths of a magnitude. The photometry was corrected for Galactic foreground reddening using the extinction values given in the RC3 catalogue (de Vaucouleurs et al. 1991).

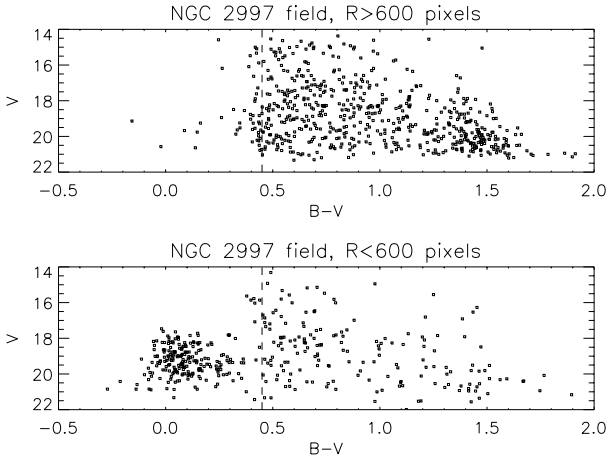

Fig. 1. Colour-magnitude diagrams for objects in the NGC 2997 field. Top: Objects at distance larger than 600 pixels (4 arcmin) from the centre of the galaxy. Bottom: Objects at distance closer than 600 pixels to the centre of the galaxy

3.3. Identification of star clusters

In short, young star cluster candidates were identified as compact bright, blue objects without any Hα emission. The specific criteria invoked to select cluster candidates were the following:

The first criterion was that the objects should have $B - V < 0.45$. In this way most foreground stars are eliminated, as demonstrated in Fig. 1 which shows colour-magnitude diagrams for objects in the field containing the galaxy NGC 2997. The NGC 2997 field is relatively rich in foreground stars, while the galaxy itself occupies only the central part of the frame, and therefore this field serves as an illustrative example. The difference between the colour-magnitude diagrams of the central part of the field (where the galaxy is located) and the outer parts (only foreground) is striking. In fact some of the foreground stars are slightly bluer than $B - V = 0.45$, so the limit is not completely rigorous and was adjusted slightly from case to case by inspecting diagrams like the one in Fig. 1. A $B - V$ colour of 0.45 for a star cluster corresponds to an age of about 500 Myr (Girardi et al. 1995), so we are really just sampling young objects.

Secondly, the cluster candidates were divided into two groups, a "red" group with $U - B > -0.4$ and a "blue" group with $U - B \leq -0.4$, and an absolute magnitude limit was applied. For a given mass, clusters in the "blue" group will be more luminous than clusters in the "red" group, and therefore a brighter magnitude cut-off could be applied to the "blue" clusters. Specifically, the limits were set to $M_V < -8.5$ for the "red" group and to $M_V < -9.5$

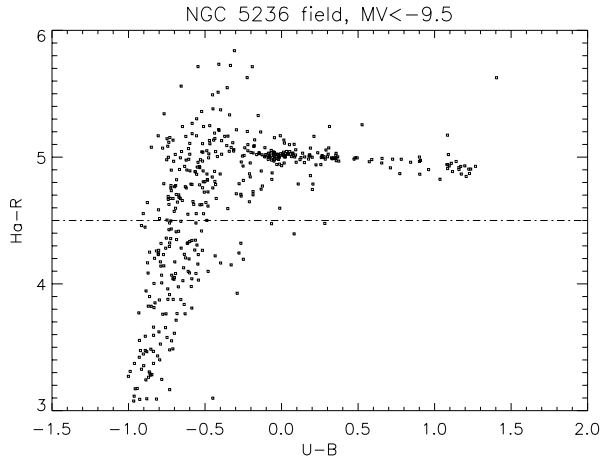

Fig. 2. $H\alpha - R$ vs. $U - B$ for objects brighter than $M_V = -9.5$ in the NGC 5236 field

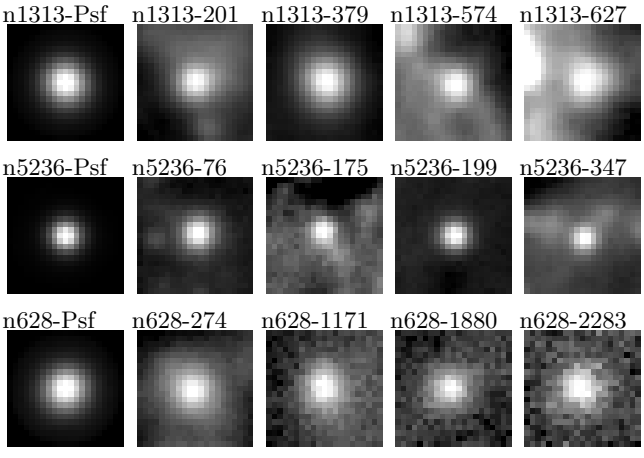

Fig. 3. V-band images of a few clusters. The first image in each row is the PSF, followed by 4 clusters

for the "blue" group (distance moduli for the galaxies are given in Paper I).

Third, it was necessary to exclude HII regions. In Fig. 2 we show $H\alpha - R$ vs. $U - B$ for all objects brighter than $M_V = -9.5$ in the NGC 5236 field, chosen as an example because of the large number of sources in this galaxy. The $H\alpha$ photometry was not standard calibrated, so the magnitude scale on the y-axis in Fig. 2 is purely instrumental. It is clear from Fig. 2 that the objects with an excess in $H\alpha$ appear around $U - B = -0.4$, while $H\alpha - R$ is rather constant for redder objects. Denoting the average $H\alpha - R$ value at $U - B > -0.4$ by $(H\alpha - R)_{\rm ref}$, we chose to cut away objects with $H\alpha - R < (H\alpha - R)_{\rm ref} - 0.5$. The limit could have been placed closer to $(H\alpha - R)_{\rm ref}$, but by choosing a cut-off at 0.5 magnitudes below $(H\alpha - R)_{\rm ref}$ we allow for some scatter in the photometry as well.

Finally we did a visual inspection of the cluster candidates. In this way objects which were too extended or "fuzzy" to be star clusters were eliminated (typically star clouds or associations in the spiral arms of the galaxies).

Photometric data are given for each cluster in Table 4, along with the effective radius $R_{\rm e}$ (in pc) as derived by **ishape** (Sect. 4). A few examples of clusters are shown in Fig. 3.

A table showing the total number of star clusters identified in each of the galaxies in our sample was given in Paper I, and we refer to that paper for a detailed discussion of the properties of the cluster systems.

4. Tools for synthetic image generation and analysis

It is a complicated problem to carry out photometry on star clusters located within spiral galaxies, partly because of the strongly varying background, and partly because the clusters are not perfect point sources. The measurements are subject to many potential errors, and it is essential to check the photometry carefully and get a realistic idea of the achievable accuracy. One way to do this is to carry out experiments with artificial objects, which can be added at any desired position in the image and remeasured using the photometric method of choice. In order to give realistic estimates of the photometric errors the artificial objects should, of course, resemble the real objects as closely as possible.

We have developed a number of tools to be used in the analysis of this type of image data. The two most important ones, which will be described below are

- **mksynth** - generates a synthetic image by adding artificial sources to a uniformly illuminated sky background.
- **ishape** - which finds the intrinsic shape of extended sources by modeling them as one of several available analytic models. The parameters of the analytic model are adjusted until the best fit between the observed profile and the model convolved with the PSF of the image is obtained.

In practice these two algorithms (together with some more general image processing functions) are built into one stand-alone programme[2], so that they can share common routines to handle user-definable parameters, read and write FITS images etc.

We have not included a task to generate the PSF itself from an image. This must be done using some other programme, such as the **psf** and **seepsf** tasks in DAOPHOT. We refer to the IRAF and DAOPHOT documentation for more details on these topics.

4.1. mksynth

This algorithm generates synthetic images which are as similar to real data as possible, including a "sky

[2] The programme containing the routines, (for historical reasons called **baolab**), is available at the following WWW address: http://www.astro.ku.dk/~soeren/baolab/

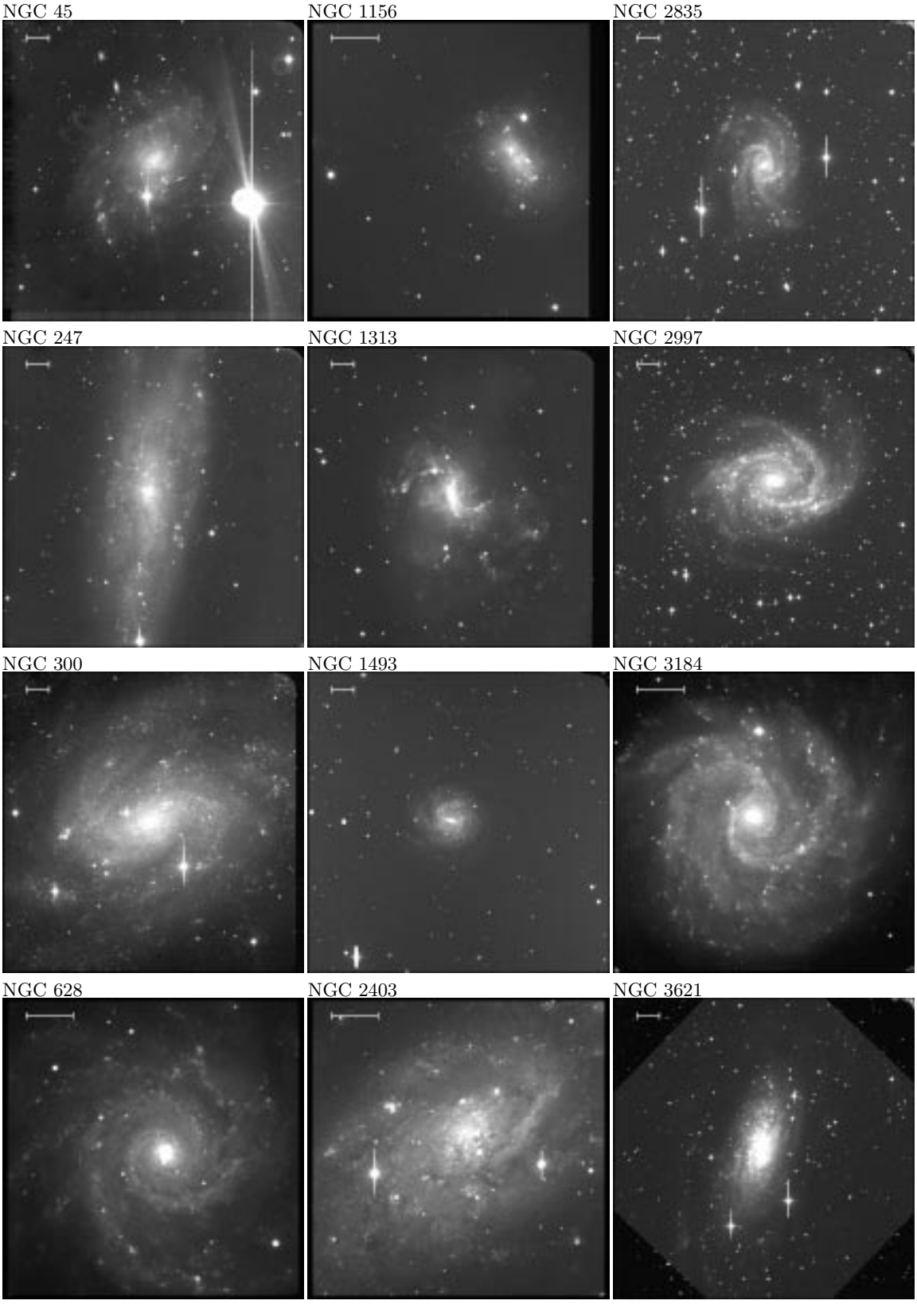

Fig. 4. V-band images of the galaxies. The bar in the upper left corner of each image corresponds to 1 arcminute. North is up and east to the left in all images

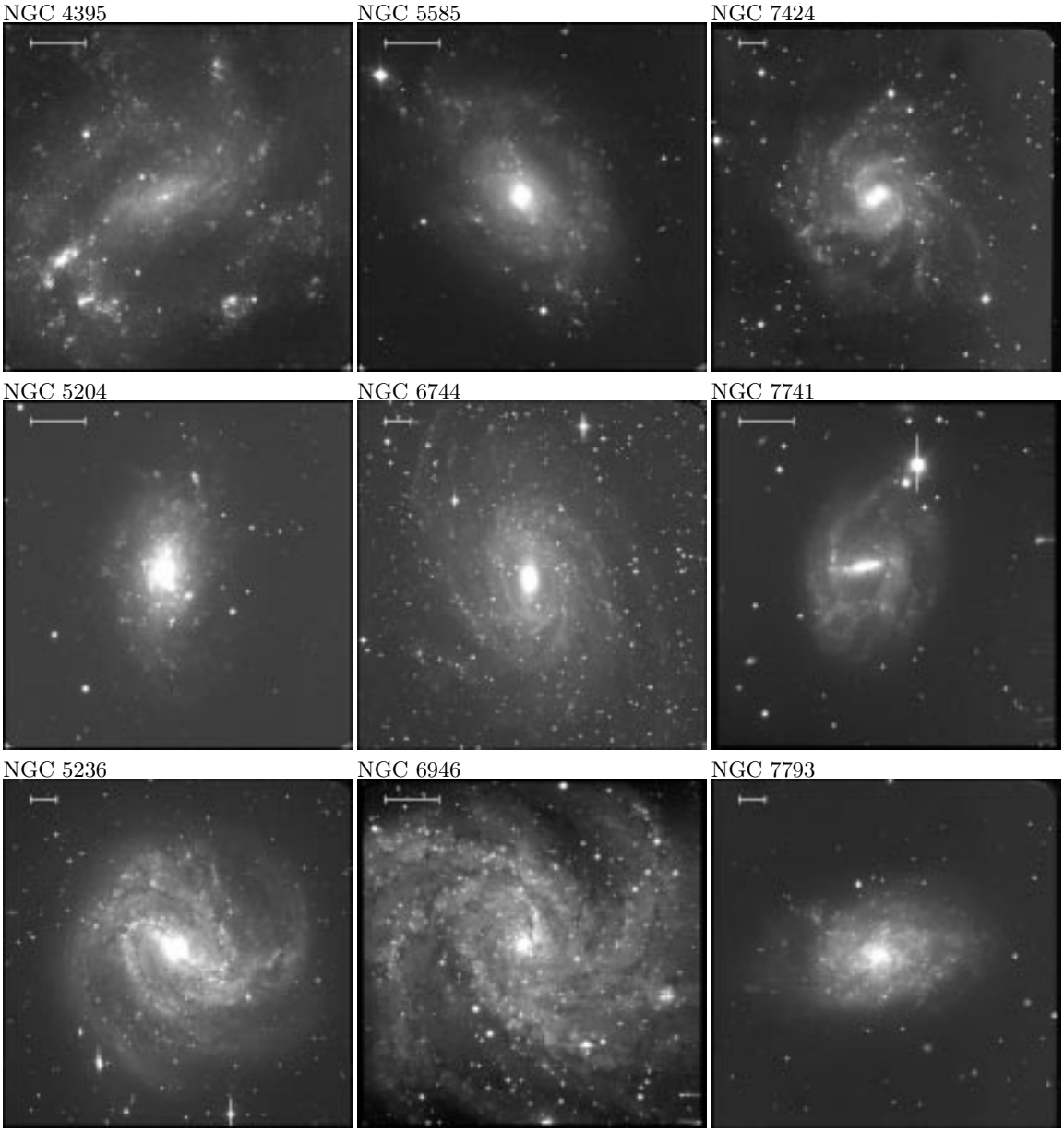

Fig. 5. See the caption to Fig. 4

background" with Gaussian photon shot noise. Stars are generated not just by adding a scaled PSF but rather by a process similar to that by which the photons arrive in a real CCD image during an integration. Thus, in contrast to other popular algorithms for adding synthetic stars to an image (such as **addstar** in DAOPHOT), **mksynth** generates a complete synthetic image from scratch, including a noisy background if desired. The PSF can be modeled as one of several analytic profiles (see Sect. 4.2), or read from a FITS file.

One of the major forces of the algorithm is that it allows a great flexibility in the generation of synthetic images, through a number of user-definable parameters. The coordinates and magnitudes of the synthetic objects can be read from a file, or generated at random.

Tests have shown that synthetic images generated by **mksynth** have very realistic noise characteristics, and it is possible to generate synthetic images which resemble real CCD images very closely. **mksynth** was described and tested more fully (although in a more primitive version) by Larsen (1996).

4.2. ishape

ishape can be used to estimate the intrinsic shape parameters of extended objects in a digital image with a known

Table 2. Essential **ishape** parameters

FITRAD = float	Fitting radius (in pixels)
CENTERRAD = float	Centering radius
CLEANRAD = float	Cleaning radius
CTRESH = float	Cleaning threshold (in σ)
SHAPE = string	Which model to use
ELLIPTICAL = YES/NO	Fit elliptical model?
EPADU = float	Conversion factor of CCD image
RON = float	Read-out noise
RESIMAGE = string	File with residual image
REPLACE = YES/NO	Remove the object from the original image?
KEEPLOG = YES/NO	Keep a log file?
LOGFILE = string	Name of log file (if KEEPLOG=YES)

PSF. The algorithm is designed to work in the domain of "slightly" extended objects which can be modeled as simple analytic functions, i.e. objects with a size roughly equal to or smaller than the PSF. Conventional deconvolution algorithms are not designed for this type of problem. None of the "first-generation" deconvolution algorithms such as the Maximum Entropy Principle (Burch et al. 1983) and the Richardson-Lucy algorithm (Richardson 1972; Lucy 1974) handled point-like sources well at all. More recent "two-channel algorithms" (Lucy 1994; Magain et al. 1998) model the image as consisting of a smoothly varying background and a number of δ-functions. The two-channel algorithms seem to work quite well in many cases, being able to separate point sources and obtain deconvolved images of photometric quality, but they are not able to treat objects which are only *nearly* point-like. Therefore we feel it is worthwhile to spend some space describing our algorithm which handles this specialised, but for our work important, case. We have used **ishape** to derive intrinsic radii for star clusters in other galaxies, but one could also imagine other areas of work where the algorithm might be useful, for example in the study of distant galaxies which are just barely resolved.

The analytic profiles by which **ishape** models the sources are:

$$\text{GAUSS: } S(z) = \exp(-z^2) \tag{1}$$

$$\text{MOFFAT15: } S(z) = \frac{1}{(1+z^2)^{1.5}} \tag{2}$$

$$\text{MOFFAT25: } S(z) = \frac{1}{(1+z^2)^{2.5}} \tag{3}$$

$$\text{KINGc: } S(z) = \begin{cases} \left(\frac{1}{\sqrt{1+z^2}} - \frac{1}{\sqrt{1+c^2}}\right)^2 & \text{for } z < c \\ 0 & \text{for } z \geq c \end{cases} \tag{4}$$

$$\text{LUGGER: } S(z) = \frac{1}{(1+z^2)^{0.9}} \tag{5}$$

$$\text{HUBBLE: } S(z) = \frac{1}{(1+z^2)} \tag{6}$$

$$\text{DELTA: } S(z) = \delta(z). \tag{7}$$

Here z is given by the equation $z^2 = a_1x^2 + a_2y^2 + a_3xy$, where the constants a_1, a_2 and a_3 depend on the major axis, ellipticity and orientation of the model, and x and y are the coordinates relative to the centre of the profile.

For the KING models, the concentration parameter[3] c may assume the values 5, 15, 30 and 100. Note that the HUBBLE model is equal to a KING model with infinite concentration parameter. The MOFFAT models are similar to the profiles used by Elson et al. (1987) to fit young LMC clusters, with their $\gamma = 3$ profile corresponding to the MOFFAT15 model and $\gamma = 5$ to the MOFFAT25 model. Elson et al. (1987) found $2.2 < \gamma < 3.2$ for their sample of LMC clusters. Unlike the KING models, the MOFFAT functions never reach a value of 0, but both the MOFFAT15 and MOFFAT25 functions share the desirable property that their volume is finite so that a well-defined effective radius exists. Clearly, the DELTA model is normally of little use, and is mostly used internally by **ishape**. The code can easily be extended to include other models as long as they can be described as simple analytic functions of the parameter z.

Denoting the observed image of an object I, the PSF with P, the intrinsic shape with S and the convolution of the two $M = P \star S$, the algorithm finds S by minimising the function:

$$\chi^2 = \sum_{i,j} W_{ij} \left[(I_{ij} - M_{ij}(x, y, a, b, w_x, w_y, \alpha))/\sigma_{ij}\right]^2 \tag{8}$$

x, y is the position of the object, a and b represent the amplitude (brightness) and the background level, and w_x, w_y and α are the $FWHM$ along the major and minor axes and the position angle. σ_{ij} is the statistical uncertainty on the pixel value at the position (i, j), and W_{ij} is a weighting function. The summation (8) is carried out over all the elements (i, j) of the image area considered (typically a rather small section around the object).

The actual implementation of the minimisation of Eq. (8) is somewhat more complicated than just minimising χ^2 as a function of all seven parameters at once, and particular care is taken to evaluate the convolution

[3] For convenience, we define the concentration parameter as $c = r_t/r_c$ where r_t is the tidal radius and r_c is the core radius. In the literature it is customary to define $c = \log(r_t/r_c)$.

$M = P \star S$ as few times as possible. Only the parameters w_x, w_y and α affect the the actual shape of the convolved profile, so one might think of χ^2 as a function of these three parameters only, with the minimisation of the remaining parameters (x, y position, the amplitude a and background b) being carried out implicitly for each choice of w_x, w_y and α. The function $\chi^2(w_x, w_y, \alpha)$ is minimised using the "downhill simplex" algorithm (Press et al. 1992) which has the advantage of being simple and robust. The initial guesses are partly user-definable, but tests have shown that as long as convergence is reached, the results are insensitive to the initial guesses.

The result of the fit is given as a $FWHM$ along the major axis and an axis ratio and orientation, but the $FWHM$ may easily be converted to an effective radius (containing half the total cluster light) for all profiles except the HUBBLE and LUGGER profiles.

Both in **mksynth** and **ishape**, the arrays containing image data are in reality stored internally with a resolution 10 times higher than the actual image resolution. However, when calculating the χ^2 (Eq. (8)) the arrays are rebinned to the original resolution.

The weighting array W is introduced in order to reduce the effect of bad pixels, cosmic ray events, nearby stars etc. The weights W are derived from the input image *before the iterations are started* by calculating the standard deviation among the pixels located in concentric rings around the centre of the object, and assigning a weight to each pixel which is inversely proportional to its deviation from the mean of the pixels located in the same ring. If the deviation of I_{ij} is smaller than one σ then the corresponding weight W_{ij} is set equal to 1, and if the deviation is larger than a user specified parameter (CTRESH) then W_{ij} is set equal to 0, effectively rejecting that pixel. For small distances from the centre of the profile the statistics will become poor and hence all weights are set equal to 1 for distances smaller than a user-specified limit (CLEANRAD). It is clear that this method of assigning weights works best for images where the sources are more or less circularly symmetric – if this is not the case, then the CLEANRAD parameter should be set to a large value so that all pixels are assigned equal weights.

Examples of the output produced by **ishape** are shown in Fig. 6. In the left part of the figure the cluster was modeled as a MOFFAT15 function, and in the right part of the figure the cluster was modeled as a DELTA function. In each set of four images the original cluster I is shown in the lower right corner, the final model convolved by the PSF (M) is seen to the lower left, the fit residuals are given to the upper left, and the weighting array W is shown to the upper right. Note how structures in the background correspond to regions that are assigned a low weight, indicated by dark areas in the weighting array. In a typical situation it would have been adequate to choose a smaller fitting radius (and thereby reduce the computation time), but in this example we have extended the fitting radius to 11 pixels in order to demonstrate how the star near the upper left corner affects the weighting array.

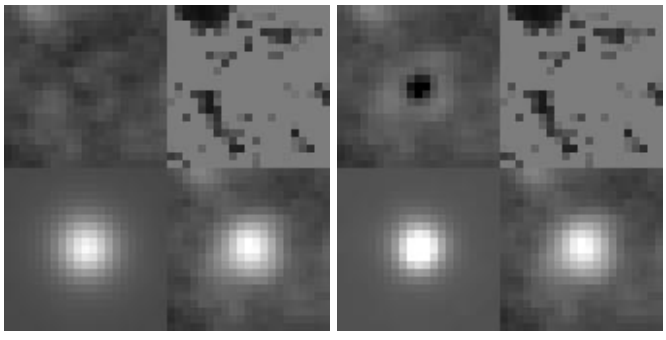

Fig. 6. Residuals from **ishape**, modeling a star cluster in NGC 5236. Left: The cluster was fitted using a MOFFAT15 model. Right: The cluster was fitted using a DELTA model

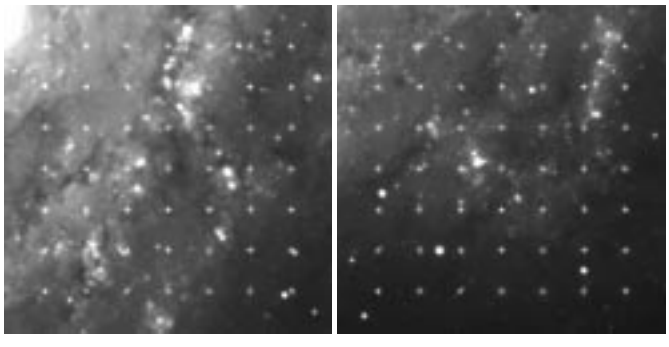

Fig. 7. The images of NGC 5236 used in the tests of **ishape**. Left: Inner field. Right: Outer field. In this figure only the images with the $m = 18.7$ objects are shown. Note that most of the artificial objects are too compact for their extent to be immediately visible

From Fig. 6 we note two things: First, the fit is improved enormously by allowing the model to be extended as opposed to the DELTA model, which corresponds to subtraction of a pure PSF. Hence, the object is clearly recognised as an extended source. Second, considering that the fitting radius in this example is as large as 11 pixels, the residuals resulting from modeling the cluster as an extended source show no other systematic variations than what can be attributed to background variations. In this particular example the $FWHM$ along the major axis of the MOFFAT15 function was found to be 1.67 pixels, and the $FWHM$ of the PSF was 4.1 pixels.

4.3. Tests of **ishape**

Before applying **ishape** to data, it is of interest to know how reliably the elongation and major axis of small objects in a CCD image can be reconstructed.

This was tested by generating a synthetic image with a number of objects with known shape parameters and then remeasuring them using **ishape**. First, 49 test

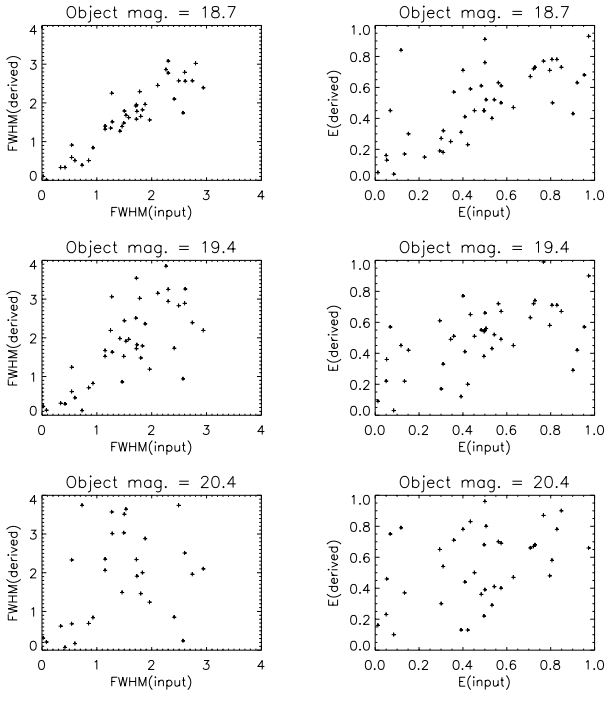

Fig. 8. Tests of **ishape** using synthetic objects added to the NGC 5236 inner field. Input $FWHM$ values in pixels (left) and axis ratios (right) are compared to the values measured by **ishape**

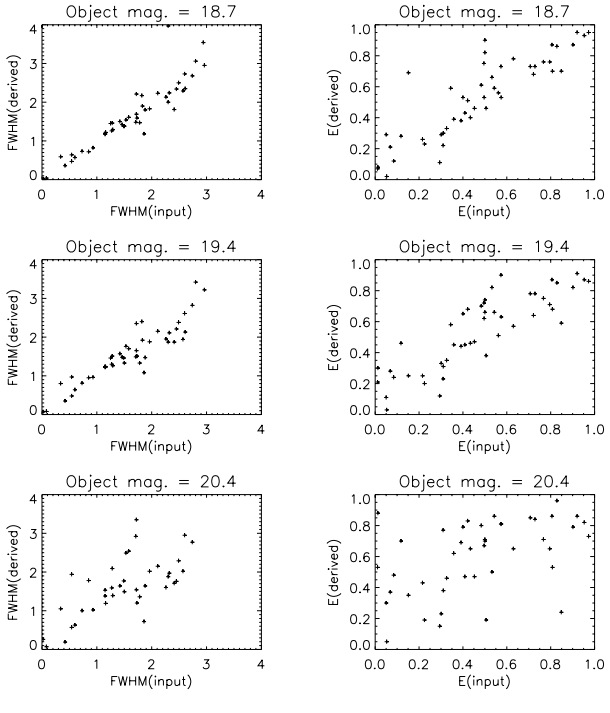

Fig. 9. Tests of **ishape** using synthetic objects added to the NGC 5236 outer field. See Fig. 8 for details

Table 3. Median S/N ratios for the data plotted in Figs. 8 and 9

Mag.	18.7	19.4	20.4
Inner field	142	79	36
Outer field	157	88	40

objects were generated by convolving the PSF measured on a V-band CCD image of the galaxy NGC 5236 with a number of MOFFAT15 models with major axis $FWHM$s in the range $0-3$ pixels and axis ratios between 0 and 1. A synthetic image with all of the 49 test objects was then generated using **mksynth**, and the synthetic image was finally added to a section of the original image of NGC 5236. This procedure was repeated for synthetic objects of magnitudes 18.7, 19.4 and 20.4 at two positions within NGC 5236 (see Fig. 7). Finally, **ishape** was run on the test images, and the shape parameters derived by **ishape** were compared with the input values.

The results are shown in Figs. 8 (inner field) and 9 (outer field). The plots in the left column show the measured $FWHM$ versus the input values, and those in the right column show the measured axis ratio versus the input values. The correlations are more tight for the outer field, implying that the high noise level and stronger background fluctuations in the bright disk near the centre of NGC 5236 limit **ishape's** ability to reconstruct the shape of the objects. The median S/N ratios for the test objects calculated by **ishape** are given in Table 3, and as expected the objects in the inner field have somewhat poorer S/N ratios. It is interesting to note that when sufficient signal is present the $FWHM$ is recovered with quite high precision even down to very small values, below $FWHM = 0.5$ pixels. The $FWHM$ of the PSF itself was 4 pixels, which means that objects with sizes as small as about 10% of that of the PSF can be recognised as extended objects with good confidence.

From Table 3 and Figs. 8 and 9 we estimate that the S/N ratio should be greater than about 50 in order to obtain reasonably accurate shape parameters, although there are probably also many other factors which affect the results, such as the presence of nearby neighbours, crowding in general and the smoothness of the background. The axis ratio is generally somewhat more uncertain than the $FWHM$, although the scatter would decrease if the more compact objects were excluded from the plot. We will not discuss axis ratios further in this paper, but remark that the elongation might be used as a criterion to look for double clusters.

In the previous tests we had the advantage of knowing the intrinsic shape of the synthetic clusters in advance. This will usually not be the case in practice, so we should also examine how sensitive the derived cluster sizes are to a particular choice of model. In this study we have used the MOFFAT15 profile to model the clusters because of its similarity to the models that were found to fit young LMC

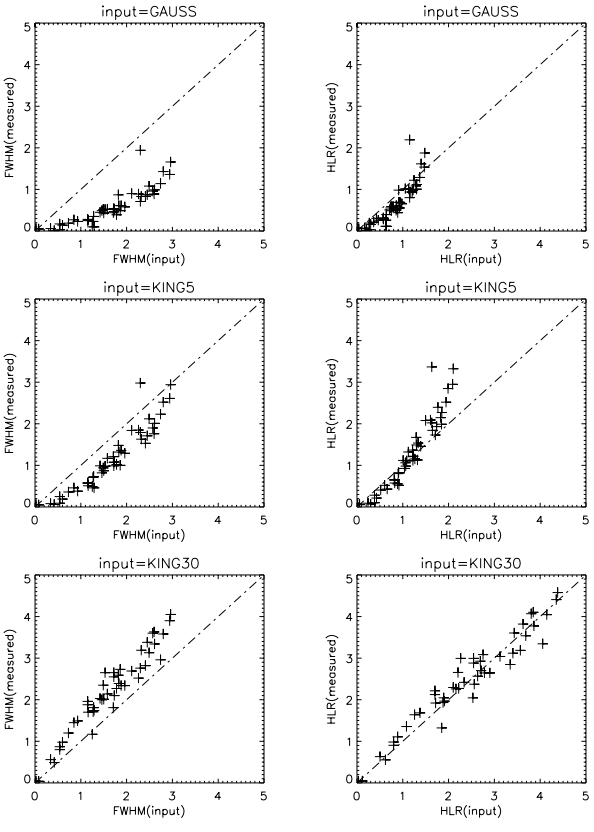

Fig. 10. The $FWHM$ and effective (half-light) radii derived from three test images by **ishape**, using a MOFFAT15 profile. The test images were generated using Gauss, King($c = 5$) and King($c = 30$) profiles. While there are obvious systematic errors in the measured $FWHM$ values (left column) when applying a wrong model, the effective radii (right column) are in fact reproduced quite well. Sizes are in pixels

clusters by Elson et al. (1987), but other choices might be as good. In particular, the classical models by King (1962) are known to fit galactic globular clusters very well. We therefore generated another set of synthetic images in the same way as for the previously described **ishape** tests, but now with Gaussian, King($c = 5$) and King($c = 30$) input models. The cluster sizes were then remeasured using **ishape** and the MOFFAT15 model. The experiment was carried out only for the outer NGC 5236 field, and for one set of images (corresponding to the brightest set used in the previous tests).

The results of this test are shown in Fig. 10 for $FWHM$ (left) and half-light radii (right). Though some systematic model dependencies are evident for the $FWHM$ values, half-light radii are reproduced quite well by the MOFFAT15 model, regardless of the input model. A related result was obtained by Kundu & Whitmore (1998) who found that effective radii derived by fits to a King model were quite insensitive to the adopted concentration parameter. We may thus conclude that the derived effective radii are not very sensitive to the choice

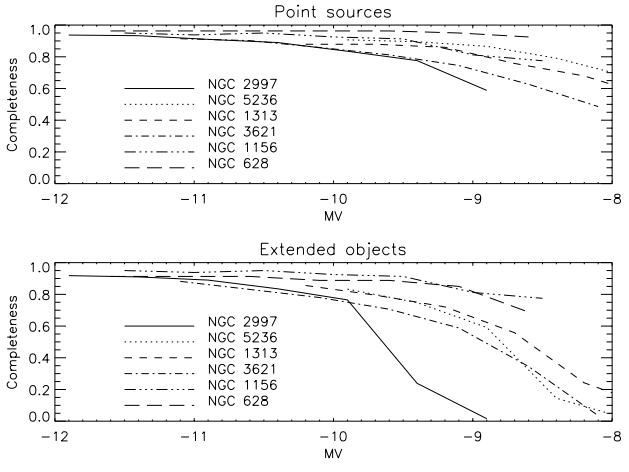

Fig. 11. Completeness corrections as a function of absolute visual magnitude M_V in six of the most cluster-rich galaxies in the sample of galaxies in Paper I. The upper panel shows the corrections applicable to point sources, while the lower panel is for extended objects with $R_{\rm e} = 20$ pc

of model, and even if the true cluster profiles are closer to King profiles the choice of the MOFFAT15 model will not introduce any large systematic errors.

5. Completeness corrections

After the discussion of software tools we now return to YMCs. In Paper I the total numbers of clusters detected in each of the 21 galaxies in our sample were listed, and we also attempted to correct the raw numbers for completeness effects. Here the completeness corrections will described in a bit more detail than in Paper I.

The fraction of clusters that are not detected may be estimated by adding artificial clusters to the images using a programme like **mksynth** and then checking how many of them are recovered by DAOFIND. This kind of completeness test is well documented in the literature for globular clusters in elliptical galaxies (Forbes 1996; Kissler-Patig et al. 1996) and also in other contexts. The artificial objects are usually added at random positions, which is a reasonable thing to do because this is also how the actual sources under study are distributed.

However, in our case the problem is somewhat different because YMCs are not distributed at random within their host galaxies. Instead, the clusters (in particular those in the "blue" group, i.e. the youngest ones) tend to be located in or near the spiral arms where they are much more likely to drown in background fluctuations, and hence a completeness test based on objects distributed at random is likely to underestimate the completeness correction.

Our approach has been to add the artificial objects "close" to the detected objects, adding 5 clusters at random positions within a radial range of $20 - 70$ pixels from each detected cluster. The objects were added to the V,

B and U band frames using the **mksynth** task, and it was then required that they were refound by **daofind** and that **phot** was able to obtain magnitudes in all three filters. The completeness tests were carried out for magnitudes down to the $M_V = -8.5$ limit at intervals of 0.5 magnitudes, and a completeness correction was then calculated for each magnitude interval. The procedure was repeated twice, for point sources and for extended objects modeled as a MOFFAT15 profile with an effective radius corresponding to $R_{\rm e} = 20$ pc convolved with the PSF. Finally, the number of clusters actually detected in each magnitude interval was corrected by the completeness correction calculated for that interval, and the corrected numbers are given in Paper I for the point-source as well for the extended-source corrections.

Completeness tests were carried out only for the galaxies with more than 20 clusters. Many of the cluster-poor galaxies contained only a handful or fewer clusters, and it makes little sense to attempt to apply completeness corrections to such small numbers.

The estimated completenesses for sources in the 6 galaxies with more than 20 clusters are shown graphically in Fig. 11 as a function of absolute visual magnitude. Note the striking difference between point sources (upper panel) and extended sources (lower panel), in particular in NGC 2997. The number of detections in NGC 2997 in the extended source experiment actually drops to 0 at $M_V = -9.0$, which indicates that in NGC 2997 we simply cannot make a realistic estimate of how many objects the galaxy contains down to a limit of $M_V = -8.5$. The other galaxies in our sample were either more nearby, or they were observed at the NOT rather than the 1.54 m telescope (and therefore with better image quality), so with the exception of two more galaxies (NGC 7424 and NGC 1493, see Paper I) the incompleteness corrections should be smaller than those for NGC 2997.

6. Resolving YMCs in the galaxies

The **ishape** algorithm was applied to all the star clusters identified as described in Sect. 3.3. For the shape model the MOFFAT15 profile was chosen because of its similarity with the models adopted by Elson et al. (1987), and the PSF was generated using DAOPHOT. The cleaning radius was set to 2 pixels and the fitting radius to 4 pixels, and the CTRESH parameter was set to 2.

The effective radii were derived both on B and V band images for the 6 most cluster-rich galaxies in order to check the results. In Fig. 12 the effective radii (in pixel units) derived by **ishape** from B and V band frames are plotted against each other for objects with $S/N > 50$, leaving out about 20% of the objects. If objects with lower S/N were included, the scatter was found to increase somewhat, although the correlations in Fig. 12 would remain evident.

As another test, radii were derived for sources in the NGC 5236 frame with $B-V > 0.6$ and $V < 19.5$. Most of these objects are expected to be foreground stars, and they are indeed distributed quite uniformly across the CCD frame. Figure 13 shows the $R_{\rm e}$ distribution for all such objects located within the central 1400×1400 pixels of the image, roughly corresponding to the area covered by the galaxy. For convenience, the effective radii have been converted to parsec. It can be seen from Fig. 13 that **ishape** finds $R_{\rm e} < 1$ pc ($0.05''$) for the vast majority of the objects with $B-V > 0.6$, in agreement with the assumption that they are in fact foreground stars. The fact that foreground stars appear virtually unresolved by **ishape** adds confidence to the algorithm's ability to recognise extended objects.

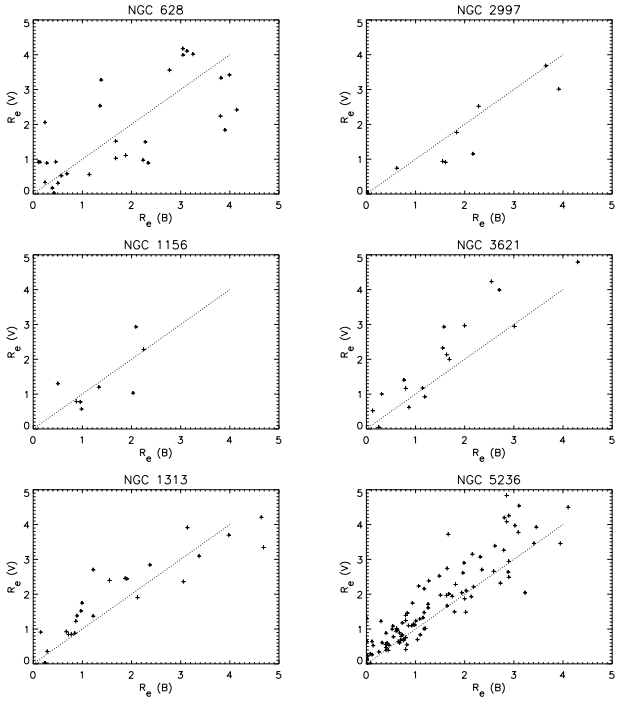

Fig. 12. The effective radii $R_{\rm e}$ in pixel units of clusters measured on V and B band frames plotted against each other. Only clusters with $S/N > 50$ are included in these plots

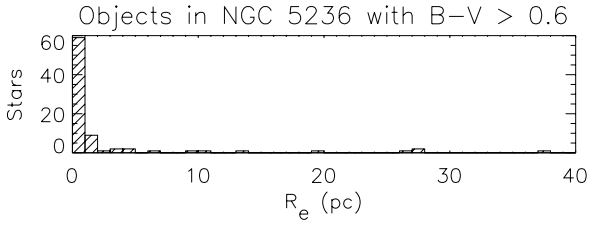

Fig. 13. Histogram of the effective radii of objects in NGC 5236 with $V < 19.5$ and $B - V > 0.6$, assumed to be mostly foreground stars. Only objects in the region $300 < x < 1700$ pixels and $300 < y < 1700$ pixels were included. For easier comparison with Fig. 14 the effective radii have been converted into parsec (1 pc $\approx 0.05''$)

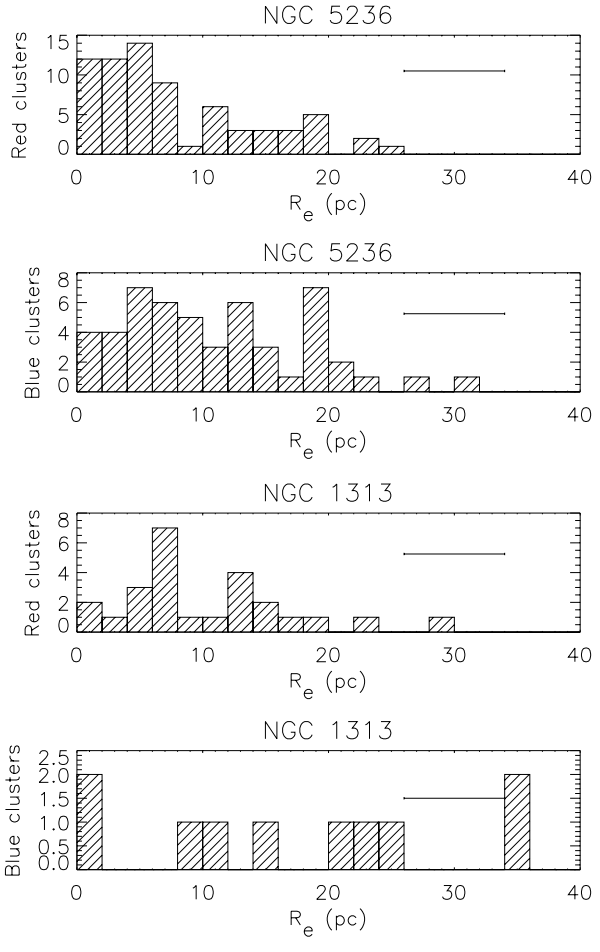

Fig. 14. Histograms of the effective radius $R_{\rm e}$ for clusters in the "red" and "blue" groups in NGC 5236 (top) and NGC 1313 (bottom). The effective radii in pixels were converted into parsec using the distances to the galaxies given in Paper I. The horizontal bar indicates the typical uncertainty

The number of clusters in most of the galaxies are really too sparse that it makes sense to discuss the $R_{\rm e}$ distributions for individual galaxies. However, Fig. 14 shows $R_{\rm e}$ histograms for two of the most cluster-rich galaxies, NGC 5236 and NGC 1313. These are also the two most nearby galaxies, at $m - M = 27.84$ and 28.2 respectively (see Paper I). Separate histograms are given for the "red" ($U - B > -0.4$) and "blue" ($U - B \leq -0.4$) cluster samples. Several systematic effects might influence the observed $R_{\rm e}$ distributions, for example the fact that the most extended clusters are detected with a much lower efficiency, and one should be careful not to overinterpret the data in Fig. 14. Nevertheless, the objects in the "blue" sample generally seem to be less concentrated, which might imply that many of the blue objects are loosely bound associations that do not survive for long, rather than bound clusters. It is emphasised, however, that this statement could only be justified by a more detailed study of the structure of the objects, something that is not feasible from ground-based observations. Figure 14 also seems to indicate that many of the objects in NGC 5236 are more concentrated than those in NGC 1313, although the statistics are poor for the latter galaxy.

From the discussion in Sect. 4.3 and Fig. 12 the uncertainty on the cluster radii is estimated to be about 0.5 pixels. 1 DFOSC pixel (0.4″) corresponds to about 7 pc at the distance of NGC 5236 and NGC 1313, so we expect an uncertainty of about 4 pc on the individual cluster radii in Fig. 14, as indicated by the horizontal error bars. The fact that we do not observe any lower limit in the $R_{\rm e}$ distribution may be an effect of the limited resolution, causing clusters with larger radii to scatter into the low $R_{\rm e}$ region, but the lower $R_{\rm e}$ limit in our sample cannot be higher than a few pc.

How do the sizes of the clusters discussed here compare with other results? Accurate measurements of cluster sizes are available only in the Milky Way and in the LMC. Most globular clusters in the Milky Way have $R_{\rm e} < 10$ pc with a peak in the $R_{\rm e}$ distribution at about 3 pc, although clusters with $R_{\rm e}$ up to ~ 30 pc exist (Harris 1996). Elson et al. (1987) found typical half-mass radii for young LMC clusters in the range $5-15$ pc, corresponding to $R_{\rm e}$ values between 4 and 12 pc (Spitzer 1987).

Effective radii have been estimated also for young clusters in the Antennae by Whitmore & Schweizer (1995, WS95) using HST/WFPC data, and in the merger remnant NGC 7252 (Whitmore et al. 1993), in both cases by assuming Gaussian cluster profiles. WS95 found an average $R_{\rm e}$ of 12 pc for the Antennae clusters, but new WFPC/2 data lead to a revised mean value of $R_{\rm e} = 4 \pm 1$ pc (Whitmore et al. 1999). In the case of NGC 7252, Whitmore et al. (1993) found a mean effective radius of 9.9 pc for clusters located at distances larger than 3.5″ from the centre of NGC 7252. Östlin et al. (1998) used the model profile of Lugger et al. (1995) to estimate *core* radii (one half times the $FWHM$) for YMCs in the blue compact galaxy ESO 338-IG04, and found a distribution that peaked at 2.5 pc with all clusters having core radii less than 10 pc. The Lugger et al. (1995) profile does not have a well-defined effective radius, but Östlin et al. (1998) also found that if the clusters were instead fitted with Gaussian profiles (for which the core radius equals $R_{\rm e}$) the core radii were about 2 times larger than for the Lugger et al. (1995) profiles, so their $R_{\rm e}$ distribution should peak at about 5 pc and have an upper limit at 20 pc.

Our observed $R_{\rm e}$ distributions thus seem to resemble those observed for YMCs in other galaxies quite well. We note, however, that the effective radii have been estimated by a variety of methods in the different studies, and this could account for some of the differences. The effective radii for the YMCs in our sample are also comparable with those of Galactic globular clusters and young LMC clusters.

The velocity dispersion in a star cluster or OB association is typically of the order of $1 - 10$ km s^{-1}, so an

unbound object will expand by $1-10$ pc/Myr. A $U-B$ colour of -0.4 corresponds to an age of about 50 Myr (Girardi et al. 1995), so most of the objects in the "red" group would have expanded to sizes much larger than what is observed and would have effectively disappeared if they were not gravitationally bound. Like all star clusters they will eventually be subject to dynamical erosion, but this acts on much longer timescales and the lifetimes are difficult to estimate without a detailed knowledge of the morphology of individual clusters and their orbits within the host galaxies.

7. Summary and conclusions

The data reductions applied to the sample of 21 galaxies presented in Paper I have been extensively discussed, in particular the algorithm **ishape** which is a useful tool for the analysis of compact objects. Tests show that **ishape** is able to recognise extended objects with good confidence, down to a $FWHM$ of about 1/10 of the $FWHM$ of the PSF itself.

Completeness tests of the cluster samples of the 6 most cluster-rich galaxies were carried out using **mksynth**, and it was demonstrated that the completeness depends strongly on the extent of the objects.

Using **ishape**, effective radii of YMCs were obtained, and the $R_{\rm e}$ distributions in NGC 1313 and NGC 5236 were studied in more detail. We found effective radii of the YMCs in these two galaxies in the range $0-20$ pc, in good agreement with results obtained for YMCs in other galaxies, and also similar to those of old globular clusters in the Milky Way and YMCs in the LMC. Some of the objects with $U-B<-0.4$ may be loosely bound associations, while objects with $U-B>-0.4$ (older than ~ 50 Myr) are orders of magnitude older than their crossing times, and we may thus conclude that they are genuine clusters. Many of them are significantly more massive than any open cluster in the Milky Way, and may well evolve into objects resembling the old globular clusters seen in the halo of the Milky Way and other galaxies today.

Acknowledgements. This research was supported by the Danish Natural Science Research Council through its Centre for Ground-Based Observational Astronomy. The valuable comments of the referee, Dr. Jon Holtzman, which helped improve this paper are appreciated. This research has made use of the NASA/IPAC Extragalactic Database (NED) which is operated by the Jet Propulsion Laboratory, California Institute of Technology, under contract with the National Aeronautics and Space Administration.

References

Burch S.F., Gull S.F., Skilling J., 1983, Computer Vision, Graphics and Image Processing 23, 113
Elson R.A.W., Fall M.S., Freeman K.C., 1987, ApJ 323, 54
Fischer P., Welch D.L., Cote P., Mateo M., Madore B.F., 1992, AJ 103, 857
Forbes D.A., 1996, AJ 112, 954
Girardi L., Chiosi C., Bertelli G., Bressan A., 1995, A&A 298, 87
Harris W.E., 1996, AJ 112, 1487
Holtzman J.A., Watson A.M., Mould J.R., et al., 1996, AJ 112, 416
King I., 1962, AJ 67, 471
Kissler-Patig M., Richtler T., Hilker M., 1996, A&A 308, 704
Kundu A., Whitmore B.C., 1998, AJ 116, 2841
Landolt A.U., 1992, AJ 104, 340
Larsen S.S., 1996, Masters Thesis. Copenhagen University Observatory
Larsen S.S., Richtler T., 1999, A&A 345, 59 (Paper I)
Lucy L.B., 1974, AJ 79, 745
Lucy L.B., 1994, in: the Restoration of HST images and Spectra II, Hanish R.J. & While R.L. (eds.)
Lugger P., Cohn H., Grindlay J., 1995, ApJ 439, 191
Magain P., Courbin F., Sohy S., 1998, ApJ 494, 472
Press W.H., Teukolsky S.A., Vetterling W.T., Flannery B.P., 1992, Numerical Recipes in C/Fortran, second ed. Cambridge University Press
Richardson W.H., 1972, J. Opt. Soc. Am. 62, 55
Spitzer L., 1987, Dynamical Evolution of Globular Clusters. Princeton University Press
Stetson P., 1987, PASP 99, 191
de Vaucouleurs G., de Vaucouleurs A., Corwin H.G., et al., 1991, Third Reference Catalogue of Bright Galaxies. Springer-Verlag New York (RC3)
Whitmore B.C., Schweizer F., Leitherer C., et al., 1993, AJ 106, 1354
Whitmore B.C., Schweizer F., 1995, AJ 109, 960 (WS95)
Whitmore B.C., Zhang Q., Leitherer C., Fall M., Schweizer F., 1999, BAAS 31, 12.05
Östlin G., Bergvall N., Rönnback J., 1998, A&A 335, 85

Table 4. Data for all the clusters identified in this study. Column 1 identifies each cluster by the name of its host galaxy and a number. E.g. "n1313-221" refers to a cluster in the galaxy NGC 1313. The column (x, y) gives the pixel coordinates of each cluster. $\alpha(2000.0)$ and $\delta(2000.0)$ are the right ascension and declination. M_V is the absolute visual magnitude and $U-B$, $B-V$ and $V-I$ are the broad-band colours. All photometric data are corrected for galactic foreground extinction. R_e is the effective radius in pc, as estimated by **ishape** using a MOFFAT15 model

ID	(x, y)	$\alpha(2000.0)$	$\delta(2000.0)$	M_V	$U-B$	$B-V$	$V-I$	R_e
n45-121	645,685	0:14:15.10	−23:13:24.9	−9.94	−0.64	0.34	0.68	32.8
n45-271	1104,1034	0:14:01.74	−23:11:12.8	−8.77	−0.14	0.43	0.66	4.7
n45-341	1030,1203	0:14:03.72	−23:10:05.8	−8.51	−0.31	0.09	0.33	27.6
n247-508	949,1057	0:47:09.29	−20:45:30.2	−8.63	−0.28	0.33	0.58	37.7
n247-871	1327,1715	0:46:58.25	−20:41:16.0	−10.24	−0.67	0.02	0.39	4.9
n247-899	985,1784	0:47:07.76	−20:40:45.5	−9.38	−0.06	0.16	0.46	6.5
n300-221	1319,342	0:54:43.48	−37:45:33.1	−8.62	−0.16	0.28	0.79	9.8
n300-566	1822,579	0:54:26.71	−37:44:03.6	−8.69	−0.35	0.18	0.42	4.7
n300-1273	393,919	0:55:13.74	−37:41:39.9	−9.85	−0.64	0.20	0.37	4.6
n628-92	1297,93	1:36:38.74	15:44:17.2	−10.52	−0.78	−0.02	0.27	12.8
n628-168	1151,170	1:36:40.63	15:44:31.3	−10.03	−0.90	−0.11	0.19	30.4
n628-201	1306,209	1:36:38.64	15:44:38.8	−8.92	−0.31	0.22	0.51	23.2
n628-274	844,306	1:36:44.61	15:44:56.2	−11.33	−0.83	0.04	0.43	10.3
n628-544	649,579	1:36:47.15	15:45:46.7	−11.31	−0.79	0.03	0.36	43.9
n628-549	1033,584	1:36:42.20	15:45:48.3	−10.01	−0.58	0.32	0.64	29.0
n628-563	1250,592	1:36:39.40	15:45:50.1	−9.84	−0.62	0.02	0.50	1.0
n628-622	1141,636	1:36:40.81	15:45:58.2	−9.65	−0.64	0.00	0.26	5.2
n628-681	1414,667	1:36:37.30	15:46:04.4	−8.59	−0.19	0.12	0.30	16.9
n628-824	1461,747	1:36:36.70	15:46:19.4	−8.61	−0.22	0.08	0.13	5.0
n628-947	1208,822	1:36:39.97	15:46:32.9	−9.80	−0.83	0.03	0.56	43.4
n628-963	447,829	1:36:49.79	15:46:33.0	−8.59	−0.36	0.09	0.33	3.2
n628-976	1485,836	1:36:36.40	15:46:36.0	−9.84	−0.42	0.12	0.61	43.5
n628-1007	1003,858	1:36:42.62	15:46:39.3	−9.94	−0.77	0.05	0.50	23.2
n628-1099	1549,898	1:36:35.58	15:46:47.7	−9.61	−0.58	0.15	0.81	17.8
n628-1101	489,899	1:36:49.25	15:46:46.1	−8.81	−0.03	0.15	0.51	3.8
n628-1140	492,921	1:36:49.22	15:46:50.2	−9.87	−0.42	0.13	0.69	1.8
n628-1171	807,941	1:36:45.16	15:46:54.5	−9.58	−0.49	0.24	0.69	17.0
n628-1285	1340,996	1:36:38.29	15:47:05.6	−9.92	−0.81	0.08	0.20	31.5
n628-1340	619,1025	1:36:47.59	15:47:09.8	−11.04	−0.75	0.01	0.50	29.1
n628-1348	603,1028	1:36:47.80	15:47:10.4	−9.61	−0.63	0.10	0.24	1.8
n628-1451	1304,1067	1:36:38.76	15:47:18.8	−10.24	−0.79	−0.01	0.22	31.5
n628-1455	1485,1069	1:36:36.43	15:47:19.4	−9.85	−0.48	0.20	0.77	8.7
n628-1559	1400,1115	1:36:37.53	15:47:27.9	−9.60	−0.53	0.09	0.52	23.8
n628-1587	1338,1130	1:36:38.33	15:47:30.6	−8.80	−0.16	0.26	0.58	17.4
n628-1591	1516,1131	1:36:36.03	15:47:31.0	−9.51	−0.67	0.07	0.67	29.0
n628-1690	1266,1195	1:36:39.26	15:47:42.6	−10.22	−0.83	−0.02	0.26	29.7
n628-1780	684,1251	1:36:46.78	15:47:52.1	−9.83	−0.62	0.07	0.33	21.1
n628-1807	1282,1268	1:36:39.07	15:47:56.2	−8.91	−0.29	0.13	0.32	13.5
n628-1828	1773,1283	1:36:32.73	15:47:59.8	−9.60	−0.46	0.13	0.47	14.3
n628-1880	965,1316	1:36:43.16	15:48:04.7	−9.12	−0.23	0.19	0.65	0.8
n628-1885	1178,1318	1:36:40.41	15:48:05.4	−9.78	−0.33	0.24	0.75	4.3
n628-1926	1040,1348	1:36:42.20	15:48:10.7	−9.65	−0.61	0.02	0.59	3.0
n628-1963	1049,1377	1:36:42.08	15:48:16.2	−10.55	−0.76	0.04	0.58	24.8
n628-2120	1142,1501	1:36:40.90	15:48:39.4	−9.90	−0.49	0.11	0.75	12.8
n628-2244	674,1614	1:36:46.95	15:48:59.7	−11.33	−0.68	0.11	0.46	3.5
n628-2283	1482,1642	1:36:36.53	15:49:06.3	−8.54	−0.22	0.21	0.46	10.5
n628-2408	1048,1830	1:36:42.15	15:49:40.6	−9.44	−0.02	0.20	0.55	2.1
n1156-296	1414,883	2:59:41.83	25:13:39.0	−9.38	−0.14	0.20	0.31	0.2
n1156-310	1333,903	2:59:42.95	25:13:42.6	−8.74	−0.05	0.26	0.69	5.8
n1156-331	1488,927	2:59:40.82	25:13:47.4	−9.68	−0.62	0.05	0.32	23.2
n1156-348	1480,944	2:59:40.93	25:13:50.6	−11.10	−0.75	0.21	0.73	33.6
n1156-356	1776,950	2:59:36.86	25:13:52.4	−9.02	−0.01	0.39	0.67	6.4
n1156-361	1482,954	2:59:40.91	25:13:52.5	−10.88	−0.83	0.05	0.57	9.7
n1156-403	1456,1005	2:59:41.27	25:14:01.9	−8.98	−0.26	0.32	0.62	8.5
n1156-433	1345,1032	2:59:42.81	25:14:06.7	−9.12	−0.20	0.37	0.80	20.8
n1156-441	1324,1041	2:59:43.10	25:14:08.3	−9.47	0.32	0.31	0.54	14.6

Table 4. continued

ID	(x, y)	α(2000.0)	δ(2000.0)	M_V	$U-B$	$B-V$	$V-I$	R_e
n1156-442	1372,1042	2:59:42.44	25:14:08.6	−9.52	−0.49	−0.01	0.29	15.2
n1156-476	1329,1067	2:59:43.03	25:14:13.2	−9.53	−0.41	0.09	0.40	3.7
n1156-496	1426,1085	2:59:41.70	25:14:16.8	−9.68	−0.65	0.10	0.47	6.4
n1156-513	1404,1099	2:59:42.01	25:14:19.3	−10.01	−0.53	0.12	0.40	7.1
n1156-549	1455,1125	2:59:41.31	25:14:24.3	−9.74	−0.12	0.25	0.48	20.7
n1156-554	1269,1129	2:59:43.87	25:14:24.6	−9.74	−0.42	0.33	0.64	24.0
n1156-555	1262,1130	2:59:43.97	25:14:24.8	−9.69	−0.72	0.04	0.39	18.9
n1156-561	1351,1133	2:59:42.74	25:14:25.5	−11.07	−0.45	0.16	0.57	14.8
n1156-610	1347,1172	2:59:42.80	25:14:32.8	−10.12	−0.51	0.22	0.85	16.3
n1156-619	1370,1181	2:59:42.49	25:14:34.5	−10.03	−0.30	0.19	0.58	87.5
n1156-657	1341,1216	2:59:42.89	25:14:41.0	−9.52	−0.58	0.07	0.59	17.8
n1156-749	1155,1349	2:59:45.48	25:15:05.4	−8.68	−0.28	0.31	1.23	9.5
n1156-763	1391,1375	2:59:42.23	25:15:10.8	−10.83	−0.47	0.17	0.68	7.0
n1313-194	1064,741	3:18:10.71	−66:31:40.3	−8.69	−0.01	0.24	0.49	7.8
n1313-195	1080,741	3:18:09.66	−66:31:40.4	−8.80	−0.29	0.22	0.60	7.5
n1313-201	1096,749	3:18:08.60	−66:31:37.3	−9.91	0.15	0.37	0.68	7.3
n1313-221	1540,777	3:17:39.42	−66:31:29.4	−11.16	−0.70	0.13	0.68	67.3
n1313-227	1499,782	3:17:42.11	−66:31:27.2	−9.53	−0.61	0.14	0.51	39.3
n1313-274	1161,877	3:18:04.18	−66:30:47.6	−8.88	−0.14	0.19	0.57	20.1
n1313-275	1031,878	3:18:12.71	−66:30:46.3	−9.57	−0.03	0.31	0.68	8.4
n1313-288	679,888	3:18:35.79	−66:30:39.7	−8.68	0.04	0.32	0.71	8.8
n1313-306	1418,911	3:17:47.28	−66:30:36.0	−8.50	−0.25	0.34	0.63	13.7
n1313-311	1408,913	3:17:47.93	−66:30:35.2	−8.79	−0.34	0.32	0.77	-
n1313-346	1009,939	3:18:14.07	−66:30:22.2	−8.68	−0.07	0.32	0.96	15.8
n1313-363	993,947	3:18:15.11	−66:30:18.9	−10.58	−0.82	−0.01	0.28	66.4
n1313-373	774,954	3:18:29.47	−66:30:14.5	−9.15	−0.19	0.13	0.49	2.4
n1313-379	1410,955	3:17:47.76	−66:30:18.7	−11.00	−0.30	0.27	0.68	17.9
n1313-383	758,956	3:18:30.52	−66:30:13.6	−9.02	−0.15	0.19	0.58	6.6
n1313-396	835,966	3:18:25.45	−66:30:10.3	−8.55	−0.01	0.31	0.84	25.9
n1313-402	816,970	3:18:26.69	−66:30:08.6	−9.14	0.23	0.44	0.83	17.4
n1313-417	1096,979	3:18:08.32	−66:30:07.1	−8.64	−0.07	0.18	0.61	0.6
n1313-420	1042,980	3:18:11.86	−66:30:06.3	−9.42	0.25	0.41	0.84	9.4
n1313-440	818,997	3:18:26.53	−66:29:58.0	−8.78	−0.20	0.23	0.42	13.9
n1313-472	1442,1019	3:17:45.59	−66:29:53.8	−8.67	−0.34	0.25	0.58	12.4
n1313-503	1097,1043	3:18:08.18	−66:29:42.0	−9.77	−0.59	0.21	0.86	2.0
n1313-518	1057,1052	3:18:10.79	−66:29:38.2	−9.72	0.02	0.35	0.66	7.1
n1313-530	825,1056	3:18:25.99	−66:29:34.9	−9.62	−0.30	0.25	0.62	10.3
n1313-540	785,1064	3:18:28.60	−66:29:31.4	−8.66	−0.24	0.20	0.45	22.5
n1313-543	641,1065	3:18:38.04	−66:29:29.9	−11.44	−0.55	0.37	0.81	28.6
n1313-551	1007,1069	3:18:14.05	−66:29:31.2	−8.87	−0.21	0.10	0.26	33.7
n1313-555	657,1073	3:18:36.98	−66:29:26.9	−10.50	−0.56	0.27	0.75	26.5
n1313-572	1089,1085	3:18:08.65	−66:29:25.5	−9.05	0.02	0.34	0.75	8.2
n1313-574	675,1085	3:18:35.79	−66:29:22.3	−9.51	−0.65	0.22	0.87	10.3
n1313-594	1068,1099	3:18:10.01	−66:29:19.8	−8.66	0.02	0.42	0.72	1.7
n1313-597	975,1101	3:18:16.10	−66:29:18.4	−10.49	−0.45	0.29	0.49	135.1
n1313-598	649,1102	3:18:37.47	−66:29:15.5	−10.82	−0.60	0.21	0.80	13.1
n1313-627	998,1127	3:18:14.56	−66:29:08.3	−9.87	−0.74	0.11	0.64	24.2
n1313-633	1022,1130	3:18:12.99	−66:29:07.3	−8.74	−0.05	0.32	0.75	28.2
n1313-648	683,1142	3:18:35.19	−66:29:00.1	−8.96	−0.27	0.22	0.37	12.0
n1313-700	851,1192	3:18:24.12	−66:28:41.7	−12.08	−0.79	0.03	0.42	-
n1313-708	818,1198	3:18:26.27	−66:28:39.1	−10.50	−0.59	0.20	0.69	16.1
n1313-709	864,1198	3:18:23.26	−66:28:39.5	−12.02	−0.84	0.02	0.39	39.7
n1313-715	850,1205	3:18:24.16	−66:28:36.6	−11.63	−0.71	0.14	0.74	46.7
n1313-724	861,1225	3:18:23.42	−66:28:28.9	−9.64	−0.54	0.38	0.86	13.4
n1313-767	666,1327	3:18:36.06	−66:27:47.3	−8.57	−0.37	0.30	0.57	5.7
n1313-780	704,1366	3:18:33.52	−66:27:32.3	−8.62	0.15	0.40	0.71	15.6

Table 4. continued

ID	(x, y)	α(2000.0)	δ(2000.0)	M_V	$U-B$	$B-V$	$V-I$	R_e
n1313-783	807,1388	3:18:26.75	−66:27:24.5	−9.70	−0.08	0.28	0.59	6.1
n1313-860	323,1857	3:18:57.76	−66:24:16.6	−9.68	−0.66	0.29	0.73	1.3
n2403-250	944,271	7:36:54.14	65:33:29.9	−8.76	−0.30	0.25	0.54	10.0
n2403-850	1108,529	7:36:49.31	65:34:18.3	−9.25	−0.31	0.27	0.37	0.9
n2403-939	708,568	7:37:01.33	65:34:24.6	−8.80	−0.27	0.33	0.38	1.1
n2403-1157	575,635	7:37:05.34	65:34:36.8	−8.72	0.07	0.44	0.42	1.6
n2403-1456	1009,720	7:36:52.35	65:34:53.6	−8.50	−0.17	0.24	0.48	4.6
n2403-1629	869,775	7:36:56.57	65:35:03.5	−9.57	−0.67	0.09	0.29	1.6
n2403-1642	859,779	7:36:56.88	65:35:04.2	−9.04	−0.34	0.37	0.58	0.1
n2403-2512	1319,1000	7:36:43.14	65:35:46.4	−8.72	−0.37	0.24	0.53	6.3
n2403-2671	1130,1036	7:36:48.83	65:35:52.7	−9.87	−0.40	0.21	17.91	5.4
n2403-2866	195,1075	7:37:16.93	65:35:57.7	−9.58	−0.51	0.26	0.82	4.3
n2403-3704	803,1257	7:36:58.74	65:36:33.0	−9.44	−0.32	0.38	0.86	5.5
n2403-4016	658,1321	7:37:03.12	65:36:44.6	−9.23	0.02	0.37	0.65	5.4
n2403-4077	1074,1336	7:36:50.62	65:36:48.4	−9.53	−0.93	−0.13	−0.13	1.8
n2403-4353	1496,1444	7:36:37.98	65:37:09.4	−8.56	−0.06	0.28	0.44	3.6
n2835-599	1137,926	9:17:49.62	−22:22:08.5	−10.07	−0.54	0.02	0.42	13.7
n2835-602	961,933	9:17:54.59	−22:22:04.3	−9.13	−0.39	0.05	−0.09	1.6
n2835-622	1097,945	9:17:50.74	−22:22:00.7	−9.39	−0.32	0.16	0.50	2.3
n2835-715	1133,1012	9:17:49.68	−22:21:34.7	−10.27	−0.47	0.24	0.52	3.9
n2835-720	951,1016	9:17:54.83	−22:21:31.7	−10.87	−0.78	0.04	0.24	22.5
n2835-742	888,1033	9:17:56.60	−22:21:24.5	−9.88	−0.50	0.02	0.39	23.7
n2835-775	973,1066	9:17:54.18	−22:21:12.2	−9.90	−0.58	0.20	0.58	21.0
n2835-788	973,1079	9:17:54.17	−22:21:07.1	−9.75	−0.52	0.28	0.71	43.2
n2835-987	869,1275	9:17:57.00	−22:19:49.3	−9.72	−0.48	0.10	0.30	21.2
n2997-263	525,594	9:45:56.27	−31:14:50.7	−10.12	0.07	0.08	0.03	0.2
n2997-360	1133,805	9:45:37.55	−31:13:32.7	−11.01	−0.66	0.08	0.28	5.1
n2997-369	1176,815	9:45:36.22	−31:13:29.1	−9.78	−0.44	0.44	1.43	31.9
n2997-376	825,830	9:45:46.95	−31:13:20.4	−10.25	−0.17	0.16	0.37	10.8
n2997-405	1211,864	9:45:35.12	−31:13:10.1	−11.33	−0.49	0.07	0.42	19.8
n2997-450	1165,929	9:45:36.49	−31:12:44.2	−9.86	0.08	0.24	−0.16	0.4
n2997-453	1345,934	9:45:30.98	−31:12:43.6	−12.77	−0.65	0.01	0.40	56.8
n2997-454	1305,937	9:45:32.21	−31:12:42.2	−9.88	−0.82	0.00	0.57	38.2
n2997-478	949,959	9:45:43.08	−31:12:30.7	−10.14	0.15	0.28	0.63	1.9
n2997-503	926,976	9:45:43.77	−31:12:23.9	−10.30	−0.27	0.10	0.15	0.2
n2997-517	939,988	9:45:43.37	−31:12:19.3	−9.97	−0.32	0.18	0.41	10.8
n2997-518	773,990	9:45:48.44	−31:12:17.2	−12.28	−0.76	0.11	0.70	29.8
n2997-519	1304,991	9:45:32.20	−31:12:20.9	−12.08	−0.56	0.09	0.41	42.2
n2997-560	1256,1054	9:45:33.63	−31:11:55.8	−10.43	−0.27	0.35	0.68	5.1
n2997-605	823,1101	9:45:46.84	−31:11:34.0	−10.97	−0.37	0.15	0.49	1.1
n2997-645	1262,1143	9:45:33.40	−31:11:20.9	−11.62	−0.53	0.03	0.31	30.0
n2997-648	909,1152	9:45:44.18	−31:11:14.6	−10.59	−0.44	0.08	0.40	14.6
n2997-651	424,1153	9:45:59.01	−31:11:10.4	−11.14	−0.10	0.26	0.50	0.4
n2997-667	655,1167	9:45:51.94	−31:11:06.7	−10.74	−0.41	−0.02	0.26	38.2
n2997-670	667,1169	9:45:51.57	−31:11:06.0	−10.33	−0.48	−0.08	0.19	35.7
n2997-679	816,1174	9:45:47.01	−31:11:05.3	−12.92	−0.66	0.05	0.34	67.6
n2997-689	1250,1189	9:45:33.74	−31:11:02.8	−11.13	−0.42	−0.00	0.43	1.1
n2997-690	674,1194	9:45:51.34	−31:10:56.3	−9.75	−0.44	−0.07	0.16	17.7
n2997-693	753,1199	9:45:48.92	−31:10:54.9	−12.63	−0.76	0.01	0.40	72.4
n2997-696	1421,1200	9:45:28.50	−31:10:59.8	−10.64	−0.32	0.12	0.38	5.3
n2997-709	656,1209	9:45:51.88	−31:10:50.2	−10.13	−0.20	0.15	0.42	15.4
n2997-715	1024,1215	9:45:40.63	−31:10:50.8	−12.23	−0.66	−0.06	0.36	28.7
n2997-717	1014,1215	9:45:40.94	−31:10:50.7	−11.68	−0.60	−0.01	0.25	14.4
n2997-723	1027,1226	9:45:40.53	−31:10:46.5	−12.23	−0.78	−0.06	0.26	40.1
n2997-738	649,1241	9:45:52.08	−31:10:37.6	−9.91	−0.46	0.05	0.16	28.9
n2997-836	1245,1344	9:45:33.80	−31:10:01.8	−11.94	−0.31	0.15	0.44	11.4

Table 4. continued

ID	(x, y)	α(2000.0)	δ(2000.0)	M_V	$U-B$	$B-V$	$V-I$	R_e
n2997-838	1260,1350	9:45:33.33	−31:09:59.6	−10.27	−0.41	0.02	0.36	8.2
n2997-999	847,1660	9:45:45.77	−31:07:54.6	−9.45	−0.16	0.33	0.31	2.3
n2997-1013	1583,1682	9:45:23.27	−31:07:51.7	−10.71	−0.25	0.16	0.32	34.0
n3184-105	1217,464	10:18:06.71	41:25:58.8	−8.81	−0.20	0.11	0.44	6.1
n3184-353	824,771	10:18:11.71	41:24:44.7	−10.49	−0.56	−0.01	0.54	15.4
n3184-383	1635,823	10:18:12.71	41:27:16.4	−9.68	−0.52	0.17	0.52	22.6
n3184-475	994,956	10:18:14.79	41:25:16.1	−8.99	−0.26	0.25	0.01	33.9
n3184-568	473,1012	10:18:15.63	41:23:38.5	−8.54	−0.30	0.00	0.38	26.2
n3184-788	1549,1159	10:18:18.24	41:26:59.6	−8.67	−0.22	0.23	0.71	32.4
n3184-870	1106,1222	10:18:19.21	41:25:36.6	−9.88	−0.27	0.14	0.52	26.1
n3184-878	1027,1231	10:18:19.34	41:25:21.8	−9.13	0.07	0.45	0.57	28.9
n3184-909	1170,1257	10:18:19.79	41:25:48.5	−8.70	−0.13	0.07	0.69	14.1
n3184-1053	1546,1399	10:18:22.21	41:26:58.6	−8.55	−0.21	0.09	0.46	16.6
n3184-1070	648,1412	10:18:22.26	41:24:10.5	−10.61	−0.56	0.00	0.27	18.8
n3184-1137	1124,1483	10:18:23.52	41:25:39.4	−8.68	−0.35	0.33	0.61	31.9
n3184-1316	855,1695	10:18:26.97	41:24:48.6	−8.68	−0.35	0.09	0.36	19.2
n3621-32	643,136	11:18:27.95	−32:54:33.3	−9.97	−0.83	−0.03	0.20	38.6
n3621-38	636,186	11:18:28.14	−32:54:13.6	−8.78	−0.22	0.27	0.43	4.7
n3621-104	479,357	11:18:32.92	−32:53:05.1	−10.15	−0.67	0.10	0.56	10.2
n3621-403	882,748	11:18:20.09	−32:50:35.1	−9.75	−0.57	0.10	0.45	17.7
n3621-474	719,814	11:18:25.12	−32:50:07.8	−8.83	0.11	0.30	0.50	0.3
n3621-478	772,816	11:18:23.47	−32:50:07.4	−10.16	−0.61	0.08	0.41	1.6
n3621-500	760,827	11:18:23.83	−32:50:03.0	−10.98	−0.69	0.08	0.44	3.9
n3621-504	1149,831	11:18:11.71	−32:50:04.7	−9.27	−0.29	0.31	0.83	11.1
n3621-510	758,834	11:18:23.89	−32:50:00.2	−10.26	−0.57	0.09	0.32	19.9
n3621-512	1114,836	11:18:12.80	−32:50:02.5	−9.28	−0.13	0.35	0.60	12.7
n3621-517	998,838	11:18:16.41	−32:50:00.7	−9.76	−0.21	0.42	0.46	25.7
n3621-528	887,844	11:18:19.87	−32:49:57.4	−10.21	−0.09	0.38	0.61	3.2
n3621-534	805,847	11:18:22.42	−32:49:55.5	−9.88	−0.39	0.14	0.51	13.0
n3621-581	806,875	11:18:22.37	−32:49:44.6	−8.53	−0.29	0.20	0.32	2.9
n3621-620	837,895	11:18:21.39	−32:49:37.0	−10.04	−0.37	0.13	0.41	29.5
n3621-793	851,964	11:18:20.91	−32:49:10.0	−11.88	−0.65	0.10	0.58	14.6
n3621-794	984,964	11:18:16.76	−32:49:11.1	−11.06	−0.49	0.40	0.99	19.0
n3621-843	827,980	11:18:21.64	−32:49:03.5	−10.82	−0.54	0.14	0.66	3.2
n3621-886	851,993	11:18:20.89	−32:48:58.6	−9.52	−0.38	0.40	0.73	25.6
n3621-926	536,1012	11:18:30.69	−32:48:48.4	−9.97	−0.83	0.02	0.29	18.3
n3621-965	543,1030	11:18:30.46	−32:48:41.4	−9.81	−0.74	−0.07	0.24	55.1
n3621-1032	842,1057	11:18:21.12	−32:48:33.4	−9.66	−0.06	0.30	0.55	3.2
n3621-1034	884,1058	11:18:19.82	−32:48:33.4	−10.74	−0.72	0.07	0.45	32.6
n3621-1106	1084,1083	11:18:13.57	−32:48:25.2	−9.44	−0.14	0.19	0.52	15.2
n3621-1113	913,1085	11:18:18.89	−32:48:23.0	−11.29	−0.56	0.32	0.59	21.6
n3621-1121	1154,1087	11:18:11.38	−32:48:24.2	−8.55	0.20	0.23	0.63	54.5
n3621-1179	1167,1112	11:18:10.96	−32:48:14.5	−9.43	−0.34	−0.10	−0.07	2.9
n3621-1211	1072,1127	11:18:13.91	−32:48:07.8	−10.34	−0.67	0.12	0.53	34.6
n3621-1261	995,1146	11:18:16.30	−32:47:59.7	−11.07	−0.57	0.21	0.40	11.1
n3621-1275	960,1150	11:18:17.39	−32:47:57.9	−11.07	−0.56	0.20	0.69	20.9
n3621-1308	1133,1167	11:18:11.98	−32:47:52.6	−10.38	−0.64	0.12	0.35	15.0
n3621-1347	871,1192	11:18:20.13	−32:47:40.6	−9.27	−0.27	0.20	0.37	15.5
n3621-1354	1008,1196	11:18:15.86	−32:47:40.2	−9.83	−0.37	0.28	0.69	29.7
n3621-1366	952,1202	11:18:17.60	−32:47:37.4	−9.82	−0.13	0.42	0.83	33.3
n3621-1383	1103,1213	11:18:12.89	−32:47:34.3	−9.28	−0.32	0.35	0.52	9.2
n3621-1389	841,1218	11:18:21.05	−32:47:30.2	−8.86	−0.37	0.15	0.46	19.3
n3621-1434	978,1251	11:18:16.76	−32:47:18.4	−10.12	−0.39	0.09	0.37	27.5
n3621-1449	1146,1259	11:18:11.52	−32:47:16.6	−10.06	−0.65	0.09	0.32	26.0
n3621-1465	962,1270	11:18:17.24	−32:47:10.8	−10.08	−0.39	0.06	0.34	15.0
n3621-1497	1082,1299	11:18:13.49	−32:47:00.4	−10.62	−0.85	−0.01	0.12	20.2

Table 4. continued

ID	(x, y)	α(2000.0)	δ(2000.0)	M_V	$U-B$	$B-V$	$V-I$	R_e
n3621-1515	1022,1311	11:18:15.35	−32:46:55.2	−10.27	−0.32	0.18	0.49	28.8
n3621-1526	1092,1329	11:18:13.15	−32:46:48.7	−10.56	−0.78	0.11	0.50	9.8
n3621-1527	1004,1330	11:18:15.90	−32:46:47.6	−10.20	−0.43	0.21	0.36	1.6
n3621-1534	1012,1336	11:18:15.64	−32:46:45.3	−10.42	−0.46	0.10	0.31	12.1
n3621-1776	1462,1732	11:18:01.37	−32:44:13.5	−8.65	−0.25	0.29	0.24	6.3
n4395-469	365,1480	12:25:54.59	33:30:47.6	−9.06	−0.08	0.27	0.39	2.1
n4395-470	1260,1480	12:25:54.67	33:33:34.1	−8.56	−0.21	0.07	0.33	7.0
n5204-128	1576,901	13:29:31.94	58:26:48.7	−9.04	−0.02	0.39	0.67	4.4
n5204-200	882,980	13:29:33.70	58:24:39.6	−8.60	−0.31	0.15	0.29	1.9
n5204-226	1154,1007	13:29:34.38	58:25:30.1	−8.89	−0.39	0.13	0.30	0.7
n5204-326	1148,1077	13:29:36.04	58:25:28.9	−9.55	−0.21	0.08	0.47	9.0
n5204-332	1204,1081	13:29:36.15	58:25:39.3	−8.68	0.36	0.36	0.53	1.5
n5204-370	916,1110	13:29:36.79	58:24:45.7	−8.55	0.25	0.30	0.37	2.3
n5204-426	1004,1159	13:29:37.96	58:25:02.0	−8.71	−0.32	0.13	0.39	7.1
n5236-76	860,259	13:37:05.59	−29:57:06.9	−9.27	0.10	0.22	0.45	8.8
n5236-77	1315,259	13:36:51.85	−29:57:10.5	−9.48	−0.25	0.42	0.55	0.1
n5236-116	739,398	13:37:09.16	−29:56:11.3	−8.79	0.09	0.22	0.46	4.0
n5236-126	892,419	13:37:04.53	−29:56:04.3	−8.59	0.13	0.30	0.60	3.4
n5236-136	903,449	13:37:04.17	−29:55:52.6	−9.77	−0.22	0.43	0.57	0.0
n5236-171	594,510	13:37:13.47	−29:55:26.2	−8.56	−0.17	0.15	0.33	5.5
n5236-175	1134,522	13:36:57.16	−29:55:25.8	−8.96	−0.35	0.15	0.70	10.6
n5236-189	680,544	13:37:10.85	−29:55:13.5	−8.85	0.17	0.26	0.41	5.6
n5236-199	1271,567	13:36:52.99	−29:55:09.2	−9.04	−0.24	0.25	0.57	1.8
n5236-207	1074,575	13:36:58.94	−29:55:04.5	−8.84	−0.01	0.44	0.72	5.3
n5236-240	639,616	13:37:12.04	−29:54:44.9	−8.69	0.20	0.34	0.60	7.6
n5236-245	1055,620	13:36:59.48	−29:54:46.7	−9.46	−0.21	0.25	0.62	5.4
n5236-249	708,629	13:37:09.95	−29:54:40.4	−9.78	−0.50	0.15	0.44	10.9
n5236-254	1687,632	13:36:40.40	−29:54:46.9	−9.94	0.18	0.33	0.50	12.9
n5236-276	1293,662	13:36:52.27	−29:54:32.1	−9.99	−0.43	0.30	0.54	22.9
n5236-279	776,664	13:37:07.88	−29:54:27.2	−9.80	−0.50	0.20	0.42	16.4
n5236-282	794,669	13:37:07.33	−29:54:25.4	−10.84	−0.69	0.05	0.36	15.9
n5236-283	1186,671	13:36:55.50	−29:54:27.7	−8.52	−0.14	0.21	0.38	8.2
n5236-288	1217,673	13:36:54.56	−29:54:27.2	−9.79	−0.11	0.18	0.44	3.3
n5236-298	653,681	13:37:11.58	−29:54:19.5	−8.65	−0.14	0.23	0.50	19.8
n5236-308	676,691	13:37:10.88	−29:54:15.8	−9.78	−0.61	0.12	0.62	22.3
n5236-341	669,722	13:37:11.07	−29:54:03.6	−9.98	−0.26	0.42	0.63	0.1
n5236-347	979,725	13:37:01.71	−29:54:04.9	−10.25	−0.59	−0.02	0.46	0.1
n5236-357	839,734	13:37:05.93	−29:54:00.2	−9.19	0.01	0.44	0.67	0.1
n5236-360	1464,737	13:36:47.06	−29:54:04.0	−9.58	−0.41	0.09	0.59	2.9
n5236-362	1190,739	13:36:55.33	−29:54:01.1	−9.35	−0.21	0.16	0.43	2.8
n5236-378	627,751	13:37:12.32	−29:53:51.8	−8.51	−0.18	0.26	0.38	4.0
n5236-402	1270,768	13:36:52.90	−29:53:50.3	−9.08	−0.37	0.33	0.50	29.1
n5236-403	1096,770	13:36:58.15	−29:53:48.1	−10.37	−0.57	0.07	0.53	6.1
n5236-406	1125,773	13:36:57.27	−29:53:47.2	−9.51	−0.51	−0.06	0.19	5.7
n5236-414	1077,782	13:36:58.72	−29:53:43.3	−9.74	−0.41	0.10	0.69	9.3
n5236-426	1078,791	13:36:58.68	−29:53:39.8	−9.66	−0.45	−0.01	0.37	16.8
n5236-431	852,797	13:37:05.50	−29:53:35.6	−9.37	−0.23	0.41	0.44	1.6
n5236-437	1354,801	13:36:50.35	−29:53:38.0	−8.91	−0.35	0.14	0.52	8.5
n5236-448	1015,813	13:37:00.57	−29:53:30.6	−9.58	−0.18	0.38	0.57	0.2
n5236-467	1292,825	13:36:52.20	−29:53:28.1	−9.60	−0.37	0.42	0.73	12.3
n5236-470	1199,826	13:36:55.01	−29:53:27.0	−8.76	−0.17	0.28	0.31	9.0
n5236-475	806,831	13:37:06.87	−29:53:21.9	−9.15	−0.35	0.21	0.70	5.1
n5236-484	1337,834	13:36:50.84	−29:53:24.9	−9.78	−0.36	0.25	0.75	8.7
n5236-487	1591,836	13:36:43.17	−29:53:26.1	−8.51	−0.30	0.26	0.64	18.9
n5236-505	894,843	13:37:04.20	−29:53:17.9	−8.96	0.21	0.42	0.76	21.0
n5236-524	1429,852	13:36:48.05	−29:53:18.6	−8.98	−0.30	0.15	0.38	19.2

Table 4. continued

ID	(x, y)	α(2000.0)	δ(2000.0)	M_V	$U-B$	$B-V$	$V-I$	R_e
n5236-531	1395,857	13:36:49.08	−29:53:16.3	−9.61	−0.38	0.08	0.41	6.1
n5236-548	493,867	13:37:16.29	−29:53:05.2	−9.61	−0.11	0.21	0.33	5.5
n5236-549	795,868	13:37:07.18	−29:53:07.3	−10.14	−0.31	0.23	0.41	16.1
n5236-552	1052,869	13:36:59.42	−29:53:08.9	−9.42	−0.33	0.39	0.80	25.3
n5236-555	1428,871	13:36:48.07	−29:53:11.1	−9.47	−0.32	0.21	0.55	5.4
n5236-572	1435,883	13:36:47.85	−29:53:06.4	−8.65	−0.10	0.44	0.90	0.6
n5236-578	1515,886	13:36:45.44	−29:53:05.9	−8.53	−0.34	0.25	0.65	5.1
n5236-613	1289,906	13:36:52.24	−29:52:56.3	−10.72	−0.61	0.05	0.21	7.8
n5236-614	1101,906	13:36:57.92	−29:52:54.8	−10.02	−0.73	−0.02	0.00	23.8
n5236-620	783,909	13:37:07.51	−29:52:51.1	−10.97	−0.78	−0.06	0.15	9.2
n5236-629	735,915	13:37:08.96	−29:52:48.3	−9.92	−0.51	−0.00	0.26	0.1
n5236-634	1165,919	13:36:55.98	−29:52:50.2	−10.59	−0.30	0.18	0.36	25.1
n5236-641	782,922	13:37:07.53	−29:52:45.9	−10.38	−0.52	0.09	0.33	14.5
n5236-645	1150,925	13:36:56.43	−29:52:47.7	−10.13	−0.35	0.29	0.45	8.1
n5236-686	671,948	13:37:10.87	−29:52:34.8	−8.71	0.28	0.45	0.71	4.8
n5236-693	940,951	13:37:02.75	−29:52:35.8	−8.67	−0.30	0.34	0.93	14.9
n5236-700	1305,956	13:36:51.73	−29:52:36.8	−11.20	−0.65	0.04	0.34	22.3
n5236-705	667,958	13:37:10.98	−29:52:30.9	−8.50	−0.33	0.16	0.33	10.8
n5236-732	801,972	13:37:06.93	−29:52:26.5	−9.62	−0.33	0.23	0.71	5.0
n5236-734	890,972	13:37:04.24	−29:52:27.2	−8.83	−0.35	0.31	0.53	23.5
n5236-745	723,977	13:37:09.28	−29:52:23.9	−10.35	−0.14	0.34	0.69	5.9
n5236-747	1009,979	13:37:00.65	−29:52:25.4	−11.12	−0.63	0.28	0.63	21.3
n5236-755	808,983	13:37:06.71	−29:52:22.2	−9.37	−0.09	0.30	0.36	5.6
n5236-759	1123,986	13:36:57.21	−29:52:23.5	−9.54	−0.26	0.36	0.57	21.3
n5236-769	666,991	13:37:10.99	−29:52:17.9	−9.05	−0.38	0.19	0.56	8.7
n5236-788	1254,1001	13:36:53.24	−29:52:18.7	−9.31	−0.04	0.42	0.48	12.5
n5236-797	1165,1005	13:36:55.93	−29:52:16.4	−10.15	−0.46	0.13	0.50	5.2
n5236-805	969,1009	13:37:01.84	−29:52:13.3	−11.70	−0.52	0.23	0.70	5.9
n5236-808	1334,1010	13:36:50.82	−29:52:15.8	−9.55	−0.86	−0.17	−0.05	30.3
n5236-821	1750,1015	13:36:38.27	−29:52:17.1	−8.87	−0.31	0.11	0.35	12.1
n5236-826	1576,1019	13:36:43.52	−29:52:14.1	−9.76	−0.76	−0.04	0.28	4.5
n5236-831	1596,1023	13:36:42.91	−29:52:12.7	−9.78	−0.75	−0.07	0.13	17.3
n5236-854	797,1036	13:37:07.01	−29:52:01.3	−9.87	−0.44	0.18	0.71	5.9
n5236-859	1169,1038	13:36:55.79	−29:52:03.5	−9.23	−0.03	0.27	0.11	0.2
n5236-894	692,1055	13:37:10.17	−29:51:53.0	−10.55	−0.33	0.16	0.53	2.9
n5236-908	689,1065	13:37:10.25	−29:51:49.1	−9.87	−0.42	0.14	0.60	0.8
n5236-944	513,1087	13:37:15.55	−29:51:39.0	−9.97	−0.18	0.22	0.58	8.0
n5236-946	1101,1090	13:36:57.81	−29:51:42.5	−9.11	0.01	0.38	0.93	12.4
n5236-947	528,1091	13:37:15.09	−29:51:37.5	−9.18	−0.13	0.15	0.45	3.1
n5236-998	1330,1119	13:36:50.88	−29:51:33.0	−9.57	−0.47	0.07	0.35	14.3
n5236-1004	450,1120	13:37:17.43	−29:51:25.5	−9.18	−0.13	0.24	0.22	2.2
n5236-1013	623,1127	13:37:12.20	−29:51:24.2	−8.79	−0.38	0.26	0.55	9.4
n5236-1061	1100,1149	13:36:57.80	−29:51:19.4	−8.55	−0.20	0.43	0.58	0.8
n5236-1063	1282,1150	13:36:52.31	−29:51:20.4	−11.52	−0.81	−0.09	0.16	6.3
n5236-1090	658,1168	13:37:11.12	−29:51:08.4	−9.59	−0.59	0.05	0.59	19.1
n5236-1091	737,1170	13:37:08.74	−29:51:08.2	−10.89	−0.77	−0.03	0.22	25.5
n5236-1104	677,1181	13:37:10.54	−29:51:03.4	−9.10	−0.30	0.14	0.17	21.0
n5236-1105	1067,1181	13:36:58.78	−29:51:06.5	−9.68	−0.67	−0.01	0.34	10.6
n5236-1109	741,1182	13:37:08.61	−29:51:03.5	−10.66	−0.31	0.13	0.42	13.4
n5236-1111	750,1182	13:37:08.34	−29:51:03.6	−11.30	−0.46	0.10	0.57	14.7
n5236-1115	710,1184	13:37:09.54	−29:51:02.5	−10.67	−0.67	0.12	0.58	20.6
n5236-1119	682,1188	13:37:10.39	−29:51:00.7	−8.98	−0.38	0.09	0.23	21.8
n5236-1180	625,1222	13:37:12.08	−29:50:46.9	−10.55	−0.64	0.02	0.32	8.7
n5236-1182	983,1222	13:37:01.28	−29:50:49.8	−11.11	−0.61	0.04	0.57	6.8
n5236-1187	1646,1224	13:36:41.28	−29:50:54.2	−8.61	0.02	0.42	0.50	16.2
n5236-1189	1132,1224	13:36:56.79	−29:50:50.2	−10.63	−0.42	0.21	0.73	21.3

Table 4. continued

ID	(x, y)	α(2000.0)	δ(2000.0)	M_V	$U-B$	$B-V$	$V-I$	R_e
n5236-1201	1547,1230	13:36:44.27	−29:50:51.1	−8.65	−0.33	0.26	0.67	5.4
n5236-1227	1692,1249	13:36:39.88	−29:50:44.7	−8.55	−0.12	0.18	0.45	3.9
n5236-1234	873,1255	13:37:04.58	−29:50:35.9	−10.17	−0.63	−0.04	0.41	7.2
n5236-1235	758,1255	13:37:08.05	−29:50:35.0	−10.98	−0.74	−0.03	0.29	13.2
n5236-1237	1396,1256	13:36:48.81	−29:50:39.7	−8.52	−0.20	0.28	0.51	0.1
n5236-1242	1375,1258	13:36:49.44	−29:50:38.7	−8.66	−0.33	0.38	0.51	12.2
n5236-1253	969,1262	13:37:01.68	−29:50:34.0	−8.80	−0.12	0.32	0.39	0.1
n5236-1273	811,1276	13:37:06.44	−29:50:27.2	−8.78	−0.26	0.34	0.47	0.1
n5236-1321	1151,1306	13:36:56.17	−29:50:18.1	−9.12	−0.17	0.14	0.56	20.1
n5236-1338	658,1318	13:37:11.03	−29:50:09.5	−9.20	0.08	0.32	0.46	10.5
n5236-1343	649,1324	13:37:11.30	−29:50:07.0	−9.22	−0.03	0.30	0.33	9.2
n5236-1351	746,1327	13:37:08.37	−29:50:06.6	−9.01	0.08	0.21	0.28	6.9
n5236-1358	1160,1331	13:36:55.88	−29:50:08.4	−9.65	−0.62	0.01	0.57	34.4
n5236-1359	766,1334	13:37:07.76	−29:50:04.1	−9.63	−0.10	0.22	0.28	24.8
n5236-1371	838,1344	13:37:05.58	−29:50:00.7	−8.78	−0.30	0.23	0.47	3.3
n5236-1373	1238,1347	13:36:53.52	−29:50:02.7	−8.95	0.10	0.28	0.47	4.6
n5236-1389	1196,1354	13:36:54.78	−29:49:59.6	−10.35	−0.44	0.08	0.46	8.7
n5236-1395	978,1358	13:37:01.35	−29:49:56.3	−9.09	−0.14	0.15	0.53	15.0
n5236-1403	742,1366	13:37:08.46	−29:49:51.3	−9.18	0.16	0.30	0.47	6.1
n5236-1428	1225,1385	13:36:53.89	−29:49:47.7	−8.66	−0.39	0.11	0.40	0.6
n5236-1442	1251,1393	13:36:53.10	−29:49:44.8	−8.79	−0.37	0.23	0.93	7.1
n5236-1467	834,1410	13:37:05.66	−29:49:34.8	−8.83	−0.26	0.30	0.71	4.5
n5236-1471	1131,1412	13:36:56.70	−29:49:36.4	−9.57	−0.39	0.17	0.53	2.9
n5236-1475	819,1414	13:37:06.11	−29:49:33.1	−9.10	−0.29	0.18	0.51	7.9
n5236-1492	872,1427	13:37:04.51	−29:49:28.4	−11.63	−0.76	−0.04	0.28	21.3
n5236-1510	1241,1437	13:36:53.37	−29:49:27.4	−10.72	−0.78	−0.07	0.36	22.8
n5236-1521	703,1448	13:37:09.59	−29:49:18.8	−9.25	−0.10	0.14	0.25	5.9
n5236-1539	1237,1458	13:36:53.48	−29:49:19.1	−9.97	−0.37	0.28	0.69	15.7
n5236-1540	1159,1461	13:36:55.83	−29:49:17.3	−9.09	−0.36	0.09	0.47	17.1
n5236-1546	960,1465	13:37:01.83	−29:49:14.2	−9.76	−0.44	0.14	0.60	12.1
n5236-1554	1231,1470	13:36:53.65	−29:49:14.4	−10.53	−0.70	−0.00	0.54	2.9
n5236-1562	956,1474	13:37:01.94	−29:49:10.6	−10.07	−0.52	0.05	0.41	6.1
n5236-1568	699,1477	13:37:09.69	−29:49:07.4	−11.31	−0.86	−0.12	0.00	11.1
n5236-1570	1247,1482	13:36:53.16	−29:49:09.8	−9.62	−0.27	0.21	0.33	0.2
n5236-1579	908,1487	13:37:03.38	−29:49:05.1	−10.46	−0.56	0.01	0.45	12.0
n5236-1584	1000,1492	13:37:00.61	−29:49:03.9	−8.77	0.05	0.30	0.53	20.7
n5236-1589	1335,1496	13:36:50.50	−29:49:05.0	−9.87	−0.25	0.42	0.53	3.1
n5236-1591	1225,1498	13:36:53.82	−29:49:03.3	−10.31	−0.58	0.15	0.35	14.1
n5236-1615	1219,1519	13:36:53.99	−29:48:55.0	−10.00	−0.66	0.04	0.34	7.1
n5236-1629	882,1531	13:37:04.14	−29:48:47.6	−9.62	−0.48	0.11	0.49	7.4
n5236-1630	1067,1532	13:36:58.56	−29:48:48.7	−8.74	0.16	0.35	0.64	2.4
n5236-1634	755,1535	13:37:07.97	−29:48:45.1	−9.63	−0.54	0.12	0.61	14.6
n5236-1660	897,1559	13:37:03.67	−29:48:36.8	−9.60	−0.65	0.05	0.54	0.1
n5236-1678	896,1573	13:37:03.69	−29:48:31.3	−9.57	−0.70	0.02	0.39	3.9
n5236-1686	1077,1582	13:36:58.23	−29:48:29.2	−10.72	−0.52	0.29	0.64	2.2
n5236-1696	1082,1594	13:36:58.07	−29:48:24.5	−11.57	−0.71	0.02	0.50	46.2
n5236-1697	1018,1597	13:37:00.00	−29:48:22.8	−9.04	−0.40	0.16	0.47	5.0
n5236-1704	902,1603	13:37:03.49	−29:48:19.5	−10.02	−0.48	0.12	0.53	9.2
n5236-1709	873,1615	13:37:04.36	−29:48:14.6	−9.39	−0.31	0.11	0.36	2.9
n5236-1716	983,1622	13:37:01.04	−29:48:12.7	−8.65	−0.29	0.21	0.58	4.0
n5236-1789	1025,1851	13:36:59.63	−29:46:43.1	−10.03	−0.25	0.44	0.56	1.0
n5585-149	490,859	14:19:42.82	56:42:07.9	−10.08	−0.23	0.17	0.38	0.5
n5585-217	857,1008	14:19:46.25	56:43:16.0	−8.97	−0.03	0.20	0.35	4.6
n5585-237	770,1044	14:19:47.05	56:42:59.8	−8.88	0.10	0.30	0.46	4.4
n5585-238	698,1046	14:19:47.08	56:42:46.4	−8.58	−0.34	0.01	0.26	6.9
n5585-265	998,1078	14:19:47.85	56:43:42.2	−10.55	−0.30	0.07	0.37	8.3

Table 4. continued

ID	(x, y)	α(2000.0)	δ(2000.0)	M_V	$U-B$	$B-V$	$V-I$	R_e
n5585-271	1064,1080	14:19:47.91	56:43:54.5	−9.66	−0.38	0.13	0.39	2.6
n5585-284	767,1090	14:19:48.09	56:42:59.2	−8.59	−0.09	0.29	0.68	4.0
n5585-285	1002,1090	14:19:48.12	56:43:43.0	−10.82	−0.55	−0.05	0.32	19.2
n5585-410	1563,1382	14:19:54.82	56:45:27.1	−9.33	−0.35	0.08	0.28	4.0
n6744-359	618,482	19:10:09.63	−63:54:45.1	−9.36	−0.28	0.15	0.41	2.0
n6744-480	1005,613	19:09:46.43	−63:53:57.0	−9.59	−0.64	0.13	0.42	40.4
n6744-692	404,819	19:10:21.89	−63:52:30.7	−8.57	−0.36	0.18	0.40	6.2
n6744-733	603,856	19:10:10.01	−63:52:18.0	−10.95	−0.79	−0.02	0.17	38.4
n6744-792	870,902	19:09:54.08	−63:52:02.3	−9.95	−0.69	0.08	0.25	18.9
n6744-802	593,916	19:10:10.52	−63:51:54.4	−8.78	−0.29	0.15	0.16	17.1
n6744-855	1305,974	19:09:28.14	−63:51:37.7	−9.65	−0.64	0.03	0.25	53.7
n6744-892	1185,1021	19:09:35.21	−63:51:18.2	−9.55	−0.40	0.10	0.27	9.9
n6744-923	1393,1051	19:09:22.82	−63:51:08.1	−9.51	−0.49	0.07	0.50	10.5
n6744-945	811,1071	19:09:57.36	−63:50:55.4	−9.24	−0.37	0.21	0.61	2.4
n6744-1111	550,1247	19:10:12.62	−63:49:43.9	−10.76	−0.78	0.07	0.44	36.9
n6744-1118	999,1254	19:09:45.96	−63:49:45.1	−10.88	−0.72	0.27	1.22	37.8
n6744-1222	1037,1365	19:09:43.57	−63:49:01.8	−10.09	−0.66	0.12	0.33	15.6
n6744-1227	715,1368	19:10:02.66	−63:48:57.9	−9.83	−0.78	0.05	0.33	37.3
n6744-1241	1045,1384	19:09:43.07	−63:48:54.4	−10.13	−0.65	0.01	0.46	37.1
n6744-1294	814,1428	19:09:56.71	−63:48:35.2	−8.65	−0.31	0.16	0.37	2.1
n6744-1302	376,1436	19:10:22.67	−63:48:28.1	−9.59	−0.69	0.11	0.37	15.0
n6744-1505	540,1689	19:10:12.60	−63:46:50.2	−9.94	−0.84	0.07	0.42	35.7
n6946-273	162,231	20:35:11.67	60:06:36.2	−9.48	−0.36	0.02	0.15	7.8
n6946-281	595,238	20:35:00.87	60:06:38.5	−10.14	−0.76	−0.02	0.27	1.5
n6946-403	1071,333	20:34:49.02	60:06:57.2	−10.08	−0.88	−0.05	0.15	22.9
n6946-494	1518,381	20:34:37.88	60:07:07.1	−9.01	0.01	0.12	0.24	5.8
n6946-550	801,404	20:34:55.78	60:07:09.9	−9.57	−0.41	0.24	0.44	5.6
n6946-601	349,429	20:35:07.06	60:07:13.6	−8.82	0.02	0.11	0.19	10.8
n6946-712	1749,472	20:34:32.13	60:07:24.5	−8.97	−0.29	−0.11	0.11	10.4
n6946-760	350,492	20:35:07.06	60:07:25.4	−11.18	−0.86	0.01	0.19	0.7
n6946-790	807,503	20:34:55.65	60:07:28.4	−8.79	0.26	0.35	0.48	5.5
n6946-873	901,540	20:34:53.32	60:07:35.5	−8.78	−0.37	0.18	0.47	12.8
n6946-907	153,558	20:35:11.99	60:07:37.2	−8.87	−0.21	0.20	0.65	0.9
n6946-918	29,565	20:35:15.09	60:07:38.3	−9.89	−0.68	0.24	0.27	6.8
n6946-1014	877,607	20:34:53.94	60:07:48.0	−10.34	−0.58	0.10	0.27	10.9
n6946-1039	876,619	20:34:53.96	60:07:50.2	−9.88	−0.73	−0.04	0.19	18.1
n6946-1091	997,635	20:34:50.95	60:07:53.5	−10.04	−0.61	0.05	0.43	13.7
n6946-1140	995,653	20:34:51.00	60:07:56.8	−9.96	−0.52	0.03	0.35	17.3
n6946-1258	1570,691	20:34:36.66	60:08:05.1	−10.42	−0.27	0.22	0.37	5.9
n6946-1347	1850,717	20:34:29.67	60:08:10.4	−9.46	−0.37	0.07	0.38	4.2
n6946-1371	1276,722	20:34:44.01	60:08:10.3	−8.85	−0.18	0.27	0.28	6.6
n6946-1447	1756,741	20:34:32.03	60:08:14.7	−13.00	−0.74	0.01	0.52	11.0
n6946-1471	1784,747	20:34:31.33	60:08:15.9	−11.30	−0.75	−0.12	0.11	18.7
n6946-1473	1726,748	20:34:32.78	60:08:16.0	−9.55	−0.62	−0.09	0.29	29.9
n6946-1490	1487,754	20:34:38.75	60:08:16.7	−10.25	−0.61	0.12	0.17	42.6
n6946-1552	1025,773	20:34:50.29	60:08:19.3	−9.81	−0.31	0.16	0.41	10.9
n6946-1561	1226,776	20:34:45.27	60:08:20.2	−10.43	−0.78	−0.01	0.12	7.2
n6946-1618	1808,793	20:34:30.74	60:08:24.5	−10.26	−0.71	0.08	0.22	18.0
n6946-1640	630,800	20:35:00.16	60:08:23.5	−9.51	−0.57	0.20	0.48	11.5
n6946-1677	645,810	20:34:59.79	60:08:25.4	−10.46	−0.69	−0.02	0.38	16.8
n6946-1678	82,810	20:35:13.84	60:08:24.1	−9.25	−0.32	0.06	0.48	8.8
n6946-1699	635,816	20:35:00.04	60:08:26.5	−10.28	−0.62	0.07	0.37	21.1
n6946-1714	862,821	20:34:54.37	60:08:27.9	−10.52	−0.76	−0.02	0.17	10.6
n6946-1738	865,830	20:34:54.30	60:08:29.6	−10.73	−0.82	−0.11	0.02	38.3
n6946-1776	202,848	20:35:10.86	60:08:31.5	−9.41	−0.07	0.35	0.53	11.7
n6946-1898	890,892	20:34:53.69	60:08:41.2	−9.94	−0.47	0.24	0.24	7.4

Table 4. continued

ID	(x, y)	α(2000.0)	δ(2000.0)	M_V	$U-B$	$B-V$	$V-I$	R_e
n6946-1989	682,930	20:34:58.90	60:08:47.9	−9.70	−0.67	−0.07	−0.07	2.7
n6946-2044	682,950	20:34:58.90	60:08:51.6	−10.32	−0.64	0.03	0.46	4.4
n6946-2064	1423,956	20:34:40.40	60:08:54.2	−9.98	−0.92	−0.13	−0.09	6.5
n6946-2074	1730,960	20:34:32.73	60:08:55.6	−8.85	−0.37	0.06	0.26	6.9
n6946-2075	1367,960	20:34:41.80	60:08:54.9	−9.44	−0.31	0.32	0.63	9.9
n6946-2210	1626,1003	20:34:35.34	60:09:03.4	−10.09	−0.86	−0.04	0.11	24.7
n6946-2215	587,1004	20:35:01.29	60:09:01.5	−10.43	−0.77	−0.06	0.11	4.1
n6946-2282	603,1025	20:35:00.90	60:09:05.4	−9.16	−0.20	0.42	1.18	10.7
n6946-2315	594,1036	20:35:01.13	60:09:07.5	−9.03	−0.27	0.27	0.47	12.9
n6946-2333	860,1042	20:34:54.48	60:09:09.2	−11.72	−0.56	0.20	0.46	4.8
n6946-2350	1484,1047	20:34:38.90	60:09:11.3	−11.40	−0.87	−0.04	0.00	8.9
n6946-2388	807,1056	20:34:55.81	60:09:11.7	−10.18	−0.57	0.22	0.38	4.6
n6946-2389	583,1056	20:35:01.41	60:09:11.2	−10.59	−0.70	−0.03	−0.06	6.4
n6946-2625	1401,1128	20:34:40.99	60:09:26.3	−10.27	−0.49	0.01	0.30	7.1
n6946-2644	606,1135	20:35:00.86	60:09:26.0	−9.65	−0.63	0.22	0.23	12.6
n6946-2655	631,1137	20:35:00.23	60:09:26.4	−9.88	−0.71	−0.06	0.20	5.3
n6946-2722	292,1153	20:35:08.71	60:09:28.6	−10.43	−0.81	0.02	0.33	9.8
n6946-2745	1542,1158	20:34:37.48	60:09:32.2	−10.04	−0.71	0.02	0.18	17.7
n6946-2775	197,1166	20:35:11.08	60:09:30.8	−9.67	−0.27	0.20	0.23	8.5
n6946-2811	1759,1175	20:34:32.06	60:09:35.8	−8.65	−0.29	0.06	0.44	14.5
n6946-2813	1112,1175	20:34:48.22	60:09:34.5	−9.82	−0.62	0.11	0.09	16.4
n6946-2825	1240,1178	20:34:45.03	60:09:35.3	−10.19	−0.68	0.01	0.50	20.0
n6946-2845	1855,1186	20:34:29.66	60:09:38.0	−8.85	−0.23	−0.01	0.27	12.6
n6946-2860	164,1189	20:35:11.91	60:09:35.1	−10.21	−0.46	0.15	0.42	5.6
n6946-2871	1028,1194	20:34:50.33	60:09:37.9	−10.23	−0.66	−0.03	0.42	9.8
n6946-2956	1625,1217	20:34:35.42	60:09:43.3	−9.15	−0.36	0.00	0.29	6.4
n6946-2981	1009,1228	20:34:50.81	60:09:44.2	−11.42	−0.75	−0.05	0.24	31.2
n6946-3014	697,1239	20:34:58.61	60:09:45.6	−9.31	−0.38	0.32	0.34	11.0
n6946-3039	1019,1246	20:34:50.57	60:09:47.6	−10.64	−0.53	0.14	0.40	20.3
n6946-3130	442,1273	20:35:04.99	60:09:51.4	−9.71	−0.38	0.02	0.07	7.1
n6946-3151	1149,1281	20:34:47.33	60:09:54.4	−9.65	−0.73	0.15	0.50	55.7
n6946-3208	978,1294	20:34:51.61	60:09:56.4	−9.82	−0.46	0.32	0.94	6.3
n6946-3274	957,1314	20:34:52.14	60:10:00.1	−9.71	−0.54	0.15	0.67	13.2
n6946-3377	1086,1350	20:34:48.92	60:10:07.1	−10.00	−0.76	−0.05	0.42	15.4
n6946-3480	647,1384	20:34:59.90	60:10:12.5	−9.70	−0.58	0.19	0.43	14.1
n6946-3490	321,1389	20:35:08.05	60:10:12.8	−9.69	−0.36	0.11	0.38	12.8
n6946-3498	1239,1392	20:34:45.11	60:10:15.3	−10.45	−0.47	0.21	0.71	24.6
n6946-3583	643,1419	20:35:00.01	60:10:19.1	−9.98	−0.75	−0.07	0.32	7.6
n6946-3607	995,1427	20:34:51.22	60:10:21.3	−10.90	−0.73	0.07	0.44	10.4
n6946-3608	969,1427	20:34:51.87	60:10:21.3	−10.09	−0.61	0.16	0.63	10.2
n6946-3665	231,1447	20:35:10.32	60:10:23.4	−9.35	−0.21	0.37	0.71	5.5
n6946-3753	178,1477	20:35:11.65	60:10:28.9	−9.97	−0.72	0.08	0.45	17.2
n6946-3756	982,1478	20:34:51.56	60:10:30.8	−11.74	−0.78	−0.12	0.32	17.3
n6946-3788	494,1487	20:35:03.76	60:10:31.4	−9.53	−0.71	−0.06	−0.17	10.2
n6946-3831	1130,1503	20:34:47.86	60:10:35.8	−11.71	−0.89	−0.13	0.01	9.7
n6946-3859	1123,1515	20:34:48.04	60:10:38.0	−11.24	−0.86	−0.04	0.26	38.5
n6946-3862	877,1517	20:34:54.19	60:10:37.9	−11.32	−0.85	−0.08	0.03	16.3
n6946-3894	872,1527	20:34:54.32	60:10:39.7	−11.03	−0.81	0.02	0.23	24.3
n6946-3979	924,1558	20:34:53.03	60:10:45.6	−10.32	−0.72	−0.11	0.34	7.4
n6946-4002	477,1565	20:35:04.21	60:10:46.0	−9.09	−0.23	0.26	0.46	1.3
n6946-4026	942,1571	20:34:52.58	60:10:48.1	−9.56	−0.60	0.06	0.48	4.8
n6946-4057	664,1579	20:34:59.54	60:10:49.0	−10.35	−0.57	−0.01	0.27	6.5
n6946-4060	42,1580	20:35:15.09	60:10:47.8	−10.96	−0.91	−0.12	0.02	11.3
n6946-4099	1475,1593	20:34:39.26	60:10:53.3	−9.00	−0.18	0.16	0.46	7.3
n6946-4150	1091,1606	20:34:48.87	60:10:54.9	−9.81	−0.75	0.01	0.17	5.1
n6946-4207	420,1622	20:35:05.65	60:10:56.5	−11.59	−0.40	0.40	0.66	4.7

Table 4. continued

ID	(x, y)	α(2000.0)	δ(2000.0)	M_V	$U-B$	$B-V$	$V-I$	R_e
n6946-4227	916,1625	20:34:53.25	60:10:58.1	−8.99	−0.37	0.10	0.32	11.0
n6946-4238	124,1627	20:35:13.05	60:10:56.7	−10.16	−0.79	0.07	0.51	13.0
n6946-4254	354,1630	20:35:07.30	60:10:57.8	−9.82	−0.78	−0.16	0.29	10.4
n6946-4309	199,1649	20:35:11.18	60:11:01.0	−9.56	−0.60	−0.12	0.04	7.9
n6946-4321	757,1652	20:34:57.23	60:11:02.8	−9.18	−0.08	0.27	0.41	5.3
n6946-4338	102,1658	20:35:13.61	60:11:02.5	−10.84	−0.79	−0.12	0.24	8.6
n6946-4359	212,1663	20:35:10.86	60:11:03.7	−11.34	−0.63	−0.01	0.29	5.0
n6946-4373	84,1669	20:35:14.06	60:11:04.5	−9.95	−0.71	−0.01	0.27	12.4
n6946-4374	477,1670	20:35:04.24	60:11:05.6	−9.51	−0.69	0.29	0.53	5.3
n6946-4414	282,1689	20:35:09.12	60:11:08.7	−10.26	−0.84	−0.06	0.32	3.6
n6946-4468	373,1708	20:35:06.85	60:11:12.4	−11.97	−0.89	−0.05	0.09	7.9
n6946-4513	878,1732	20:34:54.23	60:11:18.0	−11.52	−0.49	0.03	0.35	7.4
n6946-4532	357,1740	20:35:07.26	60:11:18.4	−10.84	−0.58	0.03	0.39	7.8
n6946-4587	1006,1776	20:34:51.04	60:11:26.5	−10.44	−0.51	0.10	0.49	11.2
n6946-4590	405,1776	20:35:06.07	60:11:25.2	−9.00	−0.18	0.20	0.19	7.6
n6946-4614	1659,1794	20:34:34.71	60:11:31.1	−11.18	−0.78	0.01	0.08	11.1
n6946-4685	1635,1848	20:34:35.33	60:11:41.2	−9.96	−0.67	0.16	0.53	10.5
n7424-84	555,522	22:57:32.70	−41:07:25.4	−11.21	−0.15	0.38	0.54	0.3
n7424-148	1052,884	22:57:15.21	−41:05:07.1	−10.76	−0.81	−0.06	0.28	72.4
n7424-151	1075,891	22:57:14.41	−41:05:04.5	−10.54	−0.72	−0.18	−0.18	61.0
n7424-154	1092,902	22:57:13.81	−41:05:00.3	−10.83	−0.72	−0.12	0.25	50.7
n7424-173	860,964	22:57:21.82	−41:04:34.3	−11.13	−0.52	0.40	0.76	42.9
n7424-214	1089,1078	22:57:13.80	−41:03:51.2	−10.21	0.14	0.23	0.45	48.4
n7424-223	859,1115	22:57:21.76	−41:03:35.0	−9.74	−0.80	−0.12	0.36	30.9
n7424-230	940,1143	22:57:18.93	−41:03:24.6	−9.39	−0.31	0.36	0.80	13.4
n7424-250	798,1215	22:57:23.81	−41:02:55.3	−11.43	−0.57	0.18	0.73	0.3
n7424-273	608,1288	22:57:30.35	−41:02:25.3	−10.12	−0.73	0.32	0.62	25.0
n7793-75	803,775	23:57:54.83	−32:36:56.6	−9.99	−0.85	0.24	0.47	6.1
n7793-82	849,789	23:57:53.39	−32:36:51.4	−9.56	−0.78	0.00	0.34	3.7
n7793-135	1092,850	23:57:45.82	−32:36:29.3	−8.91	0.04	0.30	0.70	21.1
n7793-156	768,871	23:57:55.86	−32:36:18.7	−8.56	−0.39	0.13	0.47	12.5
n7793-202	859,910	23:57:53.01	−32:36:04.1	−9.53	−0.67	0.35	1.03	10.6
n7793-207	1033,914	23:57:47.61	−32:36:03.8	−8.63	−0.18	0.08	0.33	4.2
n7793-231	702,935	23:57:57.87	−32:35:53.2	−9.89	−0.60	0.14	0.34	9.2
n7793-237	890,938	23:57:52.03	−32:35:53.4	−8.78	0.06	0.29	0.22	13.7
n7793-250	890,947	23:57:52.03	−32:35:49.9	−8.96	−0.26	0.17	0.42	15.6
n7793-277	1028,969	23:57:47.74	−32:35:42.3	−9.63	−0.64	0.02	0.20	28.8
n7793-294	1015,978	23:57:48.13	−32:35:38.6	−9.82	−0.11	0.44	0.61	6.0
n7793-298	1409,980	23:57:35.91	−32:35:40.7	−10.42	−0.47	0.03	0.43	5.4
n7793-310	651,983	23:57:59.42	−32:35:34.0	−9.86	−0.63	0.10	0.70	16.0
n7793-313	635,984	23:57:59.91	−32:35:33.5	−9.79	−0.90	−0.05	0.40	53.9
n7793-364	1067,1024	23:57:46.50	−32:35:21.0	−9.85	−0.58	0.07	0.29	5.8
n7793-371	1138,1032	23:57:44.29	−32:35:18.4	−9.57	−0.90	−0.13	0.48	40.2
n7793-463	816,1126	23:57:54.22	−32:34:39.2	−9.82	−0.66	0.04	0.62	7.6
n7793-539	610,1213	23:58:00.56	−32:34:03.7	−9.57	−0.56	0.39	0.68	9.1
n7793-545	608,1222	23:58:00.61	−32:34:00.1	−9.38	−0.27	0.30	0.39	5.1
n7793-606	932,1314	23:57:50.51	−32:33:26.5	−9.03	−0.39	0.45	0.63	8.5